Quantitative analysis of a footwall-scarp degradation complex and syn-rift stratigraphic architecture, northern Carnarvon Basin, NW Shelf, offshore Australia

Barrett, B.J.[1,2*]

Hodgson, D.M.[1]

Jackson, C.A.-L.[3]

Lloyd, C.[4]

Casagrande, J.[1]

Collier, R.E.Ll.[1]

[1] *School of Earth and Environment, University of Leeds, Leeds, LS2 9JT, UK.*

[2] *Equinor ASA, Equinor Research Centre, Arkitekt Ebbells veg 10, 7053, Ranheim, Norway.*

[3] *Basin Research Group (BRG), Department of Earth Science & Engineering, Imperial College, London, SW7 2BU, UK.*

[4] *School of Earth & Environmental Sciences, University of Manchester, Manchester, M13 9PL, UK.*

*corresponding author email: bonb@equinor.com

ABSTRACT

Interactions between footwall-, hangingwall- and axial-derived depositional systems make syn-rift stratigraphic architecture difficult to predict, and preservation of net-erosional source landscapes is limited. Distinguishing between deposits derived from fault-scarp degradation (consequent systems) and those derived from long-lived catchments beyond the fault crest (antecedent systems) is also challenging but important for hydrocarbon reservoir prospecting. We undertake geometric and volumetric analysis of a fault-scarp degradation complex and adjacent hangingwall-fill associated with an individual fault block in the northern Carnarvon Basin, NW Shelf, Australia. Fault throw, and vertical and headward erosion of the complex are measured. Seismic-stratigraphic and seismic facies analyses allow us to constrain the along-strike architectural variability of the footwall-derived fans in the hangingwall. Footwall-derived systems interacted with hangingwall- and axial-derived systems, through diversion around topography, interfingering, or successive onlap. We calculate the volume of footwall-sourced hangingwall fans for nine quadrants along the fault block, and compare this to the

volume of material eroded from the immediately up-dip fault-scarp. This analysis highlights areas of sediment bypass (excess erosion) and areas fed by sediment sources beyond the degraded fault scarp (excess hangingwall-fill). Exposure of the border fault footwall and adjacent fault terraces produced small catchments located beyond the fault crest that fed the hangingwall basin. One source persisted nearly throughout the syn-rift episode, and its location coincided with: (i) an intra-basin topographic high; (ii) a local fault throw minimum, possibly representing a breached relay ramp; (iii) increased vertical and headward erosion within the fault-scarp degradation complex; and (iv) sustained clinoform development in the immediate hangingwall. Our novel quantitative volumetric approach to identify through-going sediment input points and areas dominated by sediment bypass could be applied to other rift basin-fills. We also emphasise the need to incorporate interaction of multiple sediment sources and their resultant architecture in tectono-stratigraphic models for rift basins.

1. Introduction

Fault-scarp degradation (e.g. Underhill et al., 1997; Morley et al., 2007; Mortimer & Carrapa, 2007; Welbon et al., 2007; Elliott et al., 2012; Henstra et al., 2016; Bilal et al., 2018) typically feeds sediment into the immediate hangingwall basin to form subaerial and subaqueous fans (McLeod & Underhill, 1999; Sharp et al., 2000; Fraser et al., 2002; Stewart & Reeds, 2003). In a simple source-to-sink configuration, the size of the related catchment (Elliott et al., 2012; Bilal et al., 2018), and the stratigraphic architecture of adjacent hangingwall fans (Gawthorpe et al., 1994; 2017; Dorsey et al., 1995; Dorsey & Umhoefer, 2000; Ghinassi, 2007; Barrett et al., 2018; 2019a) relate to fault throw. However, few studies attempt an integrated assessment of footwall degradation and hangingwall architecture, and those that have are from recently active systems (e.g. Collier & Gawthorpe, 1995; Pechlivanidou et al., 2018).

Two principal sources supply material from the footwall to the hangingwall of a rift basin: 1) the immediate scarps of normal faults; i.e. consequent systems, and 2) through-going sediment inputs from established catchments located beyond the immediate fault crest, i.e. antecedent systems (Gawthorpe & Leeder, 2000). Differentiating between these two supply signals in the rock record is difficult. First, in the absence of provenance, textural maturity, and biostratigraphic data, it is challenging to determine sediment source areas and the relative ages between syn-rift units. Second, many active or inactive rifts presently exposed at the Earth's surface lack fully three-dimensional exposure of hangingwall stratigraphy and the related footwall erosional landscapes. Third, subsurface imaging of drainage catchments is rare because of the limited preservation of such erosional landscapes (e.g. Smallwood & Gill, 2002; Hartley et al., 2011; Elliott et al., 2012; Stucky de Quay et al., 2017). The ability to discriminate between these two inputs is important for understanding sediment transport to and within the basin, and also for reservoir quality assessment of hangingwall fans (Reading & Richards, 1994;

Richards et al., 1998; Leppard & Gawthorpe, 2006). We thus require an alternative method for determining the location of through-going sediment input points from seismic-stratigraphic analysis alone. Mass balancing is a common technique in large-scale source-to-sink studies (Paola & Martin, 2012; Michael et al., 2013; Hampson et al., 2014; Lin & Bhattacharya, 2017; Watkins et al., 2018). Such a pragmatic approach could be used to decipher supply signals by constraining and understanding the origin of any volume deficits between hangingwall deposits and their up-dip footwall-hosted catchments.

Although, footwall-derived depositional systems are most commonly reported (e.g. Gawthorpe et al., 1994; Leppard & Gawthorpe, 2006; Ford et al., 2007; Backert et al., 2010; Turner & Cronin, 2018), in rifts defined by prominent pre-rift topography, and in which antithetic faults, folds, and interacting fault arrays are widespread, hangingwall- and axial-derived systems can be as influential as footwall-derived systems in controlling the basin infill (Leeder et al., 1996; Jackson et al., 2011; McArthur et al., 2016a). How multiple depositional systems interact within a fault-confined basin, and how those interactions evolve with the growth of associated structural elements (e.g. secondary faults and folds), is relatively understudied (Sharp et al., 2000; Jackson et al., 2006; Lewis et al., 2015; Serck & Braathen, 2019). A better understanding of these processes is necessary to unravel the complexity of the ultimate depositional architecture of a hangingwall basin-fill.

Here, we analyse footwall degradation and associated hangingwall-fill across an individual fault block in the northern Carnarvon Basin, NW Shelf, Australia using a novel volume-balancing approach. Our aims are to: 1) assess the interaction between multiple depositional systems with different origins in a fault-confined basin and the influence of evolving rift structure on their development; 2) identify the position of footwall-derived, through-going sediment entry points in the absence of direct seismic imaging of the related catchment; 3) discuss the implications of the developed approach for hydrocarbon exploration; and 4) present a quantitatively-informed interpretation of the tectono-sedimentary evolution of the basin. This study can be used to inform other systems where the coeval, net-erosional footwall system is poorly preserved, and emphasises the need to incorporate multiple sediment sources and detailed interactions between their deposits into tectono-stratigraphic models of rift basin-fills.

2. Study area

The northern Carnarvon Basin (535 000 km^2; Fig. 1) is positioned towards the southern limit of the NW Shelf, Australia, and is bounded by the Roebuck and Canning Basins to the north-east, the southern Carnarvon Basin to the south, and the Argo, Gascoyne and Cuvier Abyssal Plains to the north and west (Hocking, 1988). Internally, the basin comprises several NE-trending, Palaeozoic-Cenozoic structural elements that accommodate a <15 km thick sedimentary succession. The Beagle, Dampier, Barrow and

Exmouth sub-basins are located in the inboard region of the basin and represent failed rift systems (Fig. 1A). The Exmouth Plateau sits outboard of these sub-basins (Stagg & Colwell, 1994; Gartrell, 2016). The Exmouth Plateau is a broad 600 km long and 300-400 km wide), relatively undeformed platform that consists of stretched continental crust that is intersected by NNE-SSW-trending, domino-style extensional faults (Exon et al., 1992). The footwalls of these faults have been exploited for hydrocarbons, with the Thebe discovery being one of the most basinward (c. 350 km offshore) on the Exmouth Plateau (Williams, 2018). The north-east dipping fault bounding this discovery that is penetrated by the Thebe-2 well and its associated hangingwall basin, is the focus in this study (Figs. 1B and 1C).

The pre-rift succession across much of the Exmouth Plateau comprises Triassic fluvio-deltaic clastics (Mungaroo Formation). This formation is eroded at the crest of the studied fault, as well as many other faults across the Exmouth Plateau (Fig. 2) (Bilal et al., 2018). The base and top of the hangingwall syn-rift package are defined by the TR30 transgressive surface and the J40 sequence boundary, respectively (Marshall & Lang, 2013; Fig. 2). These units are condensed on the footwall of the fault. Overlying the J40 surface and onlapping the degraded scarp of focus is the Late Jurassic, Dingo Claystone and Jansz Sandstone (Ellis et al., 2009).

3. Geological context

The break-up of Gondwanaland resulted in multiple phases of rifting on the NW Shelf during the Paleozoic and Mesozoic (Fig. 2). The Late Carboniferous to Early Permian was characterised by the break-away of the Sibamasu block, and resulted in the development of the Westralian Superbasin and the formation of the NE-trending structural grain that dominates the NW Shelf (Yeates et al., 1987; Bradshaw et al., 1994; Etheridge & O'Brien, 1994). Following extension, a post-rift thermal sag basin developed during the Triassic, which was punctuated by shorter periods of compression (e.g. Fitzroy Movement; Forman & Wales, 1981). During this time, a thick succession of marine to non-marine (Locker Shale and Mungaroo Formation) sediments were deposited (Longley et al., 2002; Marshall & Lang, 2013).

A major period of rifting in the Late Triassic-Jurassic (Fig. 2) was responsible for the disintegration of Argoland and the formation of the northern Carnarvon Basin sub-basins, exploiting older structural fabrics (Longley et al., 2002). The Lhasa micro-plate separated from Gondwana during the Norian (Metcalfe, 1999) and the West Burma micro-plate separated over three phases spanning the Hettangian (earliest Jurassic) to Kimmeridgian (Late Jurassic) (Longley et al., 2002). The inboard sub-basins received abundant syn-rift sediments throughout the Jurassic, accumulating a >6 km thick succession. However, the more distal part of the Exmouth Plateau was sediment starved, and a condensed (<400 m

thick) siltstone succession was deposited, represented by the Murat and Athol formations (Marshall & Lang, 2013; Gartrell et al., 2016; Bilal et al., 2018). The Oxfordian J40 SB (Marshall & Lang, 2013) defines the cessation of fault activity.

After a period of tectonic quiescence, renewed activity occurred during the Berriasian (Early Cretaceous) resulting in the separation of Greater India, deposition of the Barrow Group, and formation of the Gascoyne and Cuvier oceanic abyssal plains (Veevers, 1988; Longley et al., 2002). Valanginian-Aptian marine shales (Muderong Formation) comprise the early post-rift succession and act as regional seals to Late Triassic-Early Cretaceous hydrocarbon reservoirs (Bradshaw et al., 1988; Tindale et al., 1998). Carbonate deposition replaced siliciclastic during the Late Cretaceous (Bradshaw et al., 1994). Post-rift regional tectonic activity first occurred during the Campanian (Late Cretaceous) in response to far-field plate motion on the southern Australian margin. This activity resulted in transpressional growth of pre-existing normal faults (Bradshaw et al., 1988; Tindale et al., 1998). Subsequently, during the Neogene, collision between the Australian plate and the Java-Banda arc (SE Asia) caused inversion and reactivation of faults across the northern Carnarvon Basin (Keep et al., 1998; Hengesh & Whitney, 2016) (Fig. 2).

4. Dataset

We use a full angle PSTM (Pre-Stack Time Migrated) 3D seismic reflection dataset (HEX07B) that covers an 1800 km^2 area around the Thebe discovery, and well-log data from the Thebe-2 appraisal well (Ellis et al., 2009) (Fig. 1). The seismic reflection data were acquired in 2007 with a Bolt airgun array (2000 psi) and 8 x 3600 m streamer cables with 100 m spacing, reaching a maximum penetration of 4609.5 ms TWT. Inlines trend NW and crosslines NE, with an interval of 25 m and 12.5 m, respectively. Seismic reflection data are displayed as zero phase and with the European-Australian normal polarity convention, whereby a downwards increase in acoustic impedance corresponds to a negative reflection; i.e. 'trough-peak-trough' is presented with 'red-blue-red' colours on our seismic profiles. All seismic reflection sections are presented with c. 5x vertical exaggeration. Seismic frequency within the interval of interest (~2500 to 3200 ms TWT) ranges from 15 to 65 Hz, with an average of 40 Hz. At the Thebe-2 well the seafloor is penetrated at 1325 mTVD from MSL. Due to effects of the deep water column on velocity, average velocity data has been calculated from the seabed downwards. The average velocity at the Top Pre-Rift surface in Thebe-2 is 2064 m/s. Using that velocity, the average wavelength of the data in the interval of interest is ~34 m, which yields an estimated maximum vertical resolution of 8.5 m (λ/4) and a limit of detectability of 1.1 m (λ/30) (Widess, 1973; Kallweit & Wood, 1982). Key formation tops were interpreted from well log data and formed the basis for regional seismic mapping (Fig. 2). Data used in this study is open-access and can

be downloaded from the NOPIMS (National Offshore Petroleum Information Management System) online data repository (https://nopims.dmp.wa.gov.au/nopims).

5. Methods

In order to understand the tectono-sedimentary evolution of the basin, and to locate the position of fixed drainage systems on the footwall crests that supplied the hangingwall basin, the following steps were taken.

5.1. Stratigraphic analysis

Seismic facies changes (Table 1), bedding dips and stratal terminations (onlap, downlap, truncation) were used to distinguish 12 seismic units (A-L) in the hangingwall stratigraphy. Interpretations of seismic facies are based upon diagnostic geometries and informed by the literature on depositional environments in rift basins (subsurface, modern and exposed) (e.g. Dart et al., 1994; Ravnås & Steel, 1998; Gawthorpe et al., 2000; Leppard & Gawthorpe, 2006; Henstra et al., 2017; Muravchik et al., 2018; Barrett et al., 2019a,b; Cullen et al., 2019). Units are defined based on observations and sequence stratigraphic significance is not assumed. The top and base of each unit were mapped manually at high resolution (every inline and crossline). Mapped surfaces change character and merge laterally. As such, some seismic units interfinger in some places, whereas further along-strike they are stacked. A number of seismic units are restricted to and derived from the main border fault (from the south-east), whereas others are restricted to and derived from the north-western parts of the basin. Each seismic unit was gridded and relative volume (see section 5.3) was estimated. Seismic units were grouped into four sets bound by three key stratal surfaces (KSS1-3) that are defined by multiple stratal terminations and which can be mapped throughout the hangingwall. Each unit set represents one of four phases of basin evolution.

The 3D seismic reflection data and stratigraphic framework permitted geometrical analysis of the hangingwall stratigraphy such that footwall-derived fans could be distinguished from hangingwall dip-slope- and axial-derived depositional systems. For example, clinoforms and sloping horizons that dip basinward from the main border fault and show a radial geometry in 3D are interpreted as footwall-derived fans. Based on geometry and seismic facies, the depositional systems in the hangingwall basin were characterised and their variation along-strike and through time (i.e. stratigraphically) was assessed.

5.2. Measurement of footwall degradation

The Top Pre-Rift (Top Mungaroo Formation) surface that extends across the seismic volume was mapped to reveal the geometry of the degraded fault scarp (Figs. 3 and 4). A pseudo-surface was then extrapolated by projecting the fault plane and the trend of the uneroded footwall top surface (Fig. 3). This pseudo-surface was then used to estimate the footwall geometry prior to erosion. The difference in vertical height between the highest point on the restored footwall (projected footwall cut-off) to the highest preserved point on the fault scarp is taken as the amount of *vertical erosion*. The distance between the highest point on the restored footwall to the most headward uneroded point on the footwall top surface is taken as the amount of *headward erosion* (Fig. 3). Uncertainty in these measurements, which propagates into the associated volume calculation (see below), relates to the accuracy with which we are able to assess the pre-erosion footwall geometry. This in turn is related to how accurately we extrapolate the fault plane and uneroded footwall top surface (Fig. 3). The volume between the restored footwall pseudo-surface and the Top Pre-Rift surface represents the total amount of erosion of the fault scarp (shown in cross-section in Fig. 3). We estimated fault throw every 5 inlines (125 m) by measuring the distance between the *projected footwall cut-off* point and the *observed hangingwall cut-off* (Fig. 3). Minimum fault throw is provided through measurement from the highest preserved point on the fault scarp to the hangingwall cut-off.

5.3. Volume calculations

A volume balancing approach was developed to compare the amount of sediment in the hangingwall (V_{HW}) to the amount of material eroded from the adjacent footwall (V_{FW}). For the latter, a 3D grid was constructed between the extrapolated pseudo-surface (restored footwall crest) and the Top Pre-Rift surface (Figs. 4B and 5). From this, the eroded thickness (1D) and eroded bulk volume (3D) of sediment was calculated.

To calculate the volume of sediment in the hangingwall, the two seismic units comprising radial, basinward-dipping reflections (Units E and H), were interpreted to represent footwall-derived fans. The base and top of these units were mapped, the areas between them were gridded, and the bulk volumes were calculated using the same approach as defined above for the footwall (Fig. 6).

Because the seismic reflection data are presented in time, the output volumes are not true volumes of eroded and deposited sediment. To augment comparisons along-strike, and to avoid physically unrealistic units, a ratio is presented of hangingwall-fill to footwall erosion (V_{HW}/V_{FW}). Each millisecond (TWT) on the vertical axis of a grid cell is assumed to represent one metre in the volume calculation (a velocity of 2000 m/s). The Top Pre-Rift surface in the Thebe-2 well (in the footwall) lies at 2632 ms (TWT) in the seismic data, where checkshot data yield an average velocity of 2066 m/s (Fig.

7). This was averaged from the first checkshot below the seabed (1430m MD; 1870ms TWT seismic) to the Top Pre-Rift surface (2217m MD; 1750ms TWT seismic). One millisecond (TWT) at that depth represents 1.03 m. The interval velocity at the position of the Top Pre-Rift surface is 2182 m/s and so each millisecond (TWT) in that interval could represent up to 1.09 m (TWT). Therefore, the range of estimates for the vertical axis of a footwall grid cell based on average and interval velocities is therefore 1.03-1.09 m (Fig. 7). This is up to 10% larger than the 1 m assumption for the vertical axis of a grid cell used in the volume calculation for both the footwall and hangingwall, and so all 'volumes' represent minimum values and could be underestimated by <10%.

Another assumption is that a grid cell volume in the footwall is equivalent to one in the hangingwall, which is uncertain due to the lack of depth conversion and no wells penetrating the hangingwall. We can reduce some uncertainty by extrapolating velocity data in the footwall to the depth of the tops of the hangingwall fans to account for the expected increase in velocity with depth. The *average* velocity trend from the seabed to the Top-Pre-Rift surface is extrapolated to 3000 ms TWT. The pre-rift succession, including the gas-bearing zone below the footwall crest, are thus omitted from the velocity trend. This gives an average velocity of 2282 m/s at 3000 ms (TWT). One millisecond (WT) at this depth represents 1.14 m. Following the same approach with *interval* velocity data gives 2363 m/s at the depth equivalent to the top of the hangingwall fans. In this case, one millisecond (OWT) at this depth represents up to 1.18 m. The vertical axis of a hangingwall grid cell is between 1.14-1.18 m, and is therefore up to 15% thicker than a footwall cell, and thus may represent a larger volume of rock. Therefore, our approach likely underestimates hangingwall cell volume compared to footwall cell volume, which means any derived ratio is a minimum estimate. The hangingwall succession is also lithologically different to that in the footwall (pre-rift succession) and likely has different acoustic properties (e.g. higher or lower density, and faster or slower acoustic velocity).

Our volume balancing approach would be more effective with depth-converted data. However, no hangingwall basins are drilled across the Exmouth Plateau, meaning any velocity model-based depth conversion would be uncertain. Nonetheless, our approach could be applied to depth-converted data elsewhere, or TWT data if the appropriate uncertainties outlined above are considered.

5.3.1. V_{HW}/V_{FW} quadrant analysis

In order to identify where the greatest difference in hangingwall-fill to footwall erosion occurs, we assess ten paired quadrants, with boundaries defined by interfan areas (Fig. 6A). The volume of footwall erosion (V_{FW}), and volume of sediment in the hangingwall fans (V_{HW}), are calculated for each quadrant, with the exception of Quadrant 10; this is omitted from our analysis due to significant uncertainty in the erosion measurements in the proximity of the relay zone. Only seismic units that are confidently

interpreted to be characterised by footwall-derived hangingwall fans are included in the analysis. Other hangingwall sources are therefore not considered to contribute to the volumes calculated. There are three main assumptions and considerations in our quadrant analysis: 1) all footwall-derived material is encompassed within each hangingwall quadrant, although some finer-grained, buoyant material may have bypassed the mapped area of the fans, may have been re-distributed along-strike or may have exited the basin; 2) the degraded footwall area within each quadrant supplies the hangingwall area within the same quadrant; i.e. there is no oblique supply between quadrants; 3) all eroded material from the footwall is preserved in Units E and H. Footwall-derived components are identified in other hangingwall units that could have come from fault scarp degradation. If considered in the analysis, they would increase hangingwall relative to footwall volumes and thus would support any hangingwall excess. All assumptions yield minimum estimates for hangingwall volume in each quadrant.

The difference between V_{HW} and V_{FW}, and the V_{HW}/V_{FW} ratio, are recorded for each quadrant. Any excess volume in the hangingwall (i.e. $V_{HW} > V_{FW}$ or $V_{HW}/V_{FW} > 1$) is interpreted to be a result of through-going sediment transport from beyond the footwall crest. Any excess eroded volume in the footwall (i.e. $V_{FW} > V_{HW}$ or $V_{HW}/V_{FW} < 1$) is interpreted to be a result of sediment bypass or redistribution. Quadrants are not equal in area, but through use of a ratio, the volumes are normalised and comparisons between quadrants can be made. Volumes are not normalised in the V_{HW} -V_{FW} approach and highlight 'absolute' values of footwall erosion or hangingwall-fill excess.

6. Results

6.1. Stratigraphic framework

For the stratigraphic framework, twelve stratal units (Units A-L) are identified in the hangingwall basin, based on seismic facies (Table 1) and geometry (Table 2; Fig. 8; Fig. 9). The twelve stratal units are compiled into four sets (1-4), representing four stages of evolution of the basin. Four SE-dipping antithetic faults (AA, AB, AC and AD) striking parallel to the main border fault are identified. These faults were active at various times during rifting, based on thickness patterns in adjacent syn-rift units. For ease of description, the hangingwall basin is divided into three sub-basins (northern, central and southern; Fig. 8A). The southern and central sub-basins are separated by a topographic high that trends NW. The central and northern sub-basins encompass the strike extents of antithetic faults AA and AB, respectively. Foreset heights are provided with depth-converted estimates using a velocity of 2320 m/s, which sits in the range provided from average and interval velocity data in the footwall (2282-2363 m/s; see above; Fig. 7).

6.1.1. Unit Set 1

Unit Set 1 comprises Unit A, which is bounded by the Top Pre-Rift surface at its base and KSS1 at its top (Figs. 8and 9). KSS1 is high-amplitude and laterally continuous in the northern sub-basin, but becomes lower amplitude and more discontinuous southward. Unit A extends across the entire hangingwall basin. The unit has a maximum stratigraphic thickness of 63 ms, and thins southwards to ~40 ms. Overall, Unit A thickens towards the main border fault; at the fault centre and towards the northern fault tip, this occurs in association with NW-dipping reflections that dip steeply away from the fault (SF1b, Table 1). The reflections exhibit a clinoformal geometry and appear to be fan-shaped in 3D (SF1b); we interpret these bodies as fan deltas. Elsewhere, the unit is dominated by discontinuous, undulating reflectors, which could represent subaqueous distributary channels in a relatively shallow water environment (SF6, Table 1).

6.1.2. Unit Set 2

Unit Set 2 comprises Units B-E, and is bounded at the base by KSS1 and at the top by KSS2 (Figs. 8 and 9). KSS2 comprises two high-amplitude, laterally continuous reflections that merge down-dip. Both reflections dip towards the basin at the same stratigraphic level, one from the NW and one from the SE. KSS2 is denoted by a change of seismic facies across it and multiple downlaps from reflections above.

Unit B thickens into the main border fault and slightly into the antithetic faults, AB and AC, which are separated by a short relay zone (Fig. 8A). Unit B is dominated by slope apron (SF1a, Table 1) and turbidites (SF4, Table 1). Fan-shaped, dipping reflections stack against the footwall of the main border fault, which are ~30 ms (~35 m) high and represented by single, low frequency, high amplitude wavelets. The internal architecture of the fans is below seismic resolution. SF4 (interpreted as turbidites) is the dominant seismic facies of the depositional systems inferred to come from the west, and in this case, reflections dip gently south-eastwards. Unit C is restricted to the basin centre and comprises east- and west-dipping reflections that offlap and fill the underlying topography (Figs. 8C, 8D and 9). It is dominantly composed of low amplitude, low frequency, discontinuous reflections interpreted to be a combination of mass transport deposits in clinoform bottomsets and pelagic/hemipelagic fall-out (SF5, Table 1). Their down-dip terminations interfinger with, and downlap onto Unit B. The top of Unit C is a distinct, flat-lying, high-amplitude trough event that is downlapped by reflections within Units E and F. The unit is bowl-shaped and is thickest (53 ms) at its centre. Unit D extends across the northern and central sub-basins (Figs. 8A-E and 9), but is absent in the immediate hangingwall of the main border fault. The unit thickens into antithetic faults AB and AC (Fig. 8). Mass transport deposits and pelagic/hemipelagic fall-out comprise Unit D (SF4 and SF5, Table 1), which dip gently towards the basin, from the NW. Unit E is dominated by fan deltas and intervening slope apron deposits against the main border fault (SF1a-b, Table 1) and extends along the entire hangingwall basin (Figs. 8A and 9). The unit is thickest in the immediate hangingwall of the main border fault (~93 ms) and thins towards

the basin, pinching out 400-700 m from the fault. Overall, reflections exhibit fan-shaped, dipping, clinoform-like geometries that appear to be footwall-derived. Foresets have a maximum height of 67 ms (78 m). In the north and central sub-basins, Unit E interfingers with Unit D (e.g. Figs. 8B, 8C and 8D), but towards the southern sub-basin, where present, it is downlapped by Unit D (Figs. 8E and 9). Unit E is used for volume balancing with footwall degradation because it is one of two units that are dominated by large-volume, footwall-derived fans.

6.1.3. Unit Set 3

Unit Set 3 comprises Units F-H, and is bound by KSS2 at the base and KSS3 at the top (Figs. 8 and 9). KSS3 is characterised by multiple onlaps from reflections within Unit Set 4 above. Unit F extends across the northern and central sub-basins from the West, but does not reach the main border fault. The unit thickens into antithetic faults AB, AC, and AD, and it is dominated by possible deep-water deposits (SF4 and 5; Table 1). Foresets have a maximum height of 40 ms (46 m) and dip away from antithetic fault AC, towards the south-east. Unit G extends across most of the hangingwall basin, but is absent <700 m from the main border fault because it onlaps underlying, fan delta-related topography (Unit E). The unit has a distinct character in the northern sub-basin, comprising three clinoform-bearing packages separated by a relatively flat-lying, low-medium amplitude reflection (Figs. 10E and 10F). Foresets within these units are ~20 ms tall (23 m), with clinoforms prograding southwards from the northern fault tip (SF2, Table 1; Fig. 10). In the central sub-basin, the thickness of the clinoform packages decreases, and the flat-lying horizons converge where they onlap KSS2. South of the basinal high separating the central and southern sub-basins, another set of clinoforms (SF3; ~40-60 ms; 46-70 m high) prograde south-eastwards from antithetic fault AC (Table 1; Fig. 10B). The clinoforms onlap and interfinger with the distal margin of fans within Unit H, decreasing in height down-dip (Figs. 8D and 10B). Unit H extends along the immediate hangingwall of the main border fault in the central and southern sub-basins. Similar to Unit E, Unit H comprises large (foreset heights up to 98 ms; 114 m), footwall-derived fans (SF1a-b, Table 1) that generally dip north-westward, and pinch-out ~850 m away from the fault. Unit H interfingers with the south-east dipping Unit G. Unit H is used for volume balancing with footwall degradation because, like Unit E, it contains a substantial volume of footwall-derived deposits.

6.1.4. Unit Set 4

Unit Set 4 comprises Units I-L. The unit set is bounded by KSS3 at the base and the Top Syn-Rift surface (J40 SB) at the top (Figs. 8 and 9). Only Unit I is present in the central and northern sub-basins. In the central sub-basin, it is downlapped and overlain by Unit J, and fills the topography formed by underlying units (i.e. Units G and H). Unit I comprises possible turbidites and pelagic/hemipelagic fall-out, deposited in a relatively deepwater environment (SF7, Table 1). In the most northerly part of the central sub-basin, the top of Unit J is defined by J40 SB, whereas in the southern part of the central sub-

basin the unit is downlapped by Unit K. Unit J comprises a thickened area (~2.5 km radius) positioned at the centre of the main border fault and that onlaps onto underlying topography. Steeply-dipping reflections extend ~800 m away from the centre of the main border fault in Quadrant 6, where most footwall scarp degradation is observed (see below). The unit is characterised by SF1a and SF8, which represents low-medium amplitude, high frequency (50-80 Hz), steeply-dipping reflections with a planar slope geometry, interpreted to be slope apron or submarine fan deposits. Dipping reflections are up to 100 ms (~116 m) high. Unit K is mostly limited to the southern sub-basin and is characterised by possible deepwater deposits (SF4 and SF5, Table 1). Gently dipping reflections downlap Unit G, and dip away from the main border fault towards the NW. Unit L is only present in the southern sub-basin and the top of Unit L is defined by J40 SB. The unit has a maximum thickness of 80 ms, where it fills pre-existing lows in topography and is characterised by deep water deposits (SF7 and SF8, Table 1).

6.2. Along-strike variability of hangingwall fans

Footwall-, hangingwall- and axial-derived fans are identified in the hangingwall basin based upon the dip of related seismic reflections and their overall 3D geometries. Hangingwall-derived fans refer to those sourced from the hangingwall dip-slope (from the NW). These types of fans range in geometry and stacking patterns from aggradational clinoforms with distinct topsets (SF3, Table 1) in the southern sub-basin (Unit G, Fig. 8F), to progradational foresets with limited topset development (SF2, Table 1) in the central sub-basin (Unit F, Fig. 8E). Axial-derived fans also lack topsets, have lower foreset heights (20-40 ms; 23-46 m), and occur in three, vertically stacked packages that are internally defined by strongly progradational stacking (Table 1 and Fig. 9).

Substantial variability is observed between footwall-derived fans that prograde away from the main border fault. More specifically, four along-strike variations are observed: 1) overall 3D geometry, 2) the change in 3D geometry through time, 3) internal character, and 4) stacking patterns.

The overall 3D geometry of the fans varies along-strike and is used to distinguish SF1a (planar-slightly concaved slope, interpreted to be slope aprons) from SF1b (clinoformal shape with clear topsets and foresets, interpreted to be fan deltas) (Table 1). Both geometries appear to have developed during the deposition of Units E and H (Fig. 11). Interfan areas (Barrett et al., 2019b; Fig. 10C; position II, Fig. 11A) exhibit concave reflections, as opposed to the sloping or convex to clinoformal shapes of the flanking fans.

The evolution of the fans through time commonly results in a change in their 3D geometry. Small, isolated fans (~40 ms; 46 m foreset height) are observed in Unit Set 1, which built away from the footwall of the main border fault. In Unit Sets 2 and 3, individual fans enlarge (e.g. ~250 m radius; ~114 m foreset heights) and coalesce, occupying ~90% of the main border fault length. Slope apron

deposits develop between the fans (e.g. positions III, IV, V and VI, Fig. 11A). Towards the northern end of the fault, fan size does not increase through time. Positions III, IV, VI, IX and XI (Figs. 11A and 11B) show a change from a clinoformal geometry in the lower units to a sloping geometry in Units E and H. The only position that maintains its clinoformal geometry throughout its development is position VII (Figs. 11A and 11B).

The internal seismic character of the fans, in particular internal reflection continuity, is also variable along-strike from chaotic (e.g. positions IV and V, Fig. 11A), through discontinuous (e.g. positions III, X and XI, Fig. 11A), to continuous (e.g. positions I, VI, IX and VIII, Fig. 11A). The seismic character is also variable through time. For example, at position VII (Fig. 11A), reflectivity is continuous towards the base, discontinuous in the middle, chaotic within a short interval, before becoming continuous again towards the top (Fig. 11B).

In the lower units, stacking patterns of clinoforms change from progradational towards the north-eastern fault tip (position I, Fig. 11A) to aggradational towards the fault centre (position IV, Fig. 11A). At position VII, where a clinoform-like geometry is maintained throughout rifting, stacking varies between progradational, aggradational, and retrogradational trends through time (Fig. 11B). Even with the absence of a topset-foreset breakpoint for stacking analysis, a strong retrogradational trend is clearly visible ~1 km to the south (position VIII, Fig. 11B), and an aggradational trend ~2 km to the north (position VI, Fig. 11B). This variability likely reflects the delicate balance between accommodation creation and sediment supply along the fault.

6.3. Footwall analysis results

The most accurate estimation of fault throw is presented with measurements from the projected footwall cut-off (red line, Fig. 12A), although there is some uncertainty with the mapping of the pseudo-surface. Measurements from the highest point on the preserved fault scarp represent the minimum fault throw (grey line, Fig. 12A). Both show a parabolic trend along-strike. Maximum fault throw (projected) is measured towards the fault centre (642 ms; 424 m), decreasing to c. 170 ms (198 m) towards the fault tips. Measurements do not reach the fault tips because the north-eastern fault tip is beyond the seismic dataset limit, and in the south-west, the fault extends into a relay zone with an adjacent fault and the fault tip position is obscured. A fault throw minima is observed in Q7 (Figs. 6 and 12), which coincides with a topographic high in the hangingwall that separates the central and southern sub-basins (Fig. 9). The high appears to be inherited from an underlying, perpendicular structure. The fault throw minima suggests that this position could represent a now-breached relay zone.

Minimum values of vertical erosion are apparent towards the fault tips (23 ms; 24 m using a velocity of 2066 m/s), increasing towards the fault centre with an approximate parabolic distribution along-strike,

in line with fault throw. The maximum vertical erosion (228 ms; 236 m) is in Q6 (Figs. 6 and 12A); this coincides with maximum headward erosion (905 m). Headward erosion is highly irregular along-strike, with large differences between peaks and troughs over short distances. Notable peaks in headward erosion occur in Q3 and Q5-7 (Fig. 12A). Nonetheless, there is still also an overall parabolic trend along the fault, in line with fault throw. Drainage systems in the footwall could be indicated by positions of high headward erosion, but distinct thalwegs, such as those documented in Elliott et al. (2012) were not clear in the seismic reflection data. Moreover, beyond the fault scarp degradation complex, the hangingwall dip slope is conformable until the next across-strike fault, thus an erosional landscape beyond the footwall crest is not apparent; either it did not form, or it was not preserved. This highlights the requirement for an alternative method to identify fixed, through-going sediment input points.

6.4. Volume balancing - V_{HW}/V_{FW}

Volume balancing between the footwall-derived material in the hangingwall fans (V_{HW} of Units E and H) and the eroded material from the footwall (V_{FW}) reveals the position of through-going sediment input points, and areas of sediment bypass and/or redistribution. More specifically, quadrants that exhibit excess footwall erosion relative to hangingwall-fill ($V_{HW}/V_{FW} < 1$) represent areas of sediment bypass, and those that exhibit excess hangingwall-fill ($V_{HW}/V_{FW} > 1$) correspond to through-going, antecedent sediment input points. In the V_{HW}/V_{FW} plot (Fig. 12B), many of the quadrants show values close to 1, indicating an approximate balance between erosion and adjacent sedimentation. In the V_{HW} -V_{FW} plot, balanced quadrants have a value close to 0. Using both plots, the only area of convincing sediment bypass is in Q5, which coincides with an area characterised by the deposition of hangingwall slope aprons (Fig. 11). Areas with apparent sediment bypass may in fact be balanced if stratigraphically older fans, buried more deeply within the hangingwall, were included in the hangingwall volume calculation.

The highest peak in V_{HW}/V_{FW} and V_{HW} -V_{FW} occurs in Q6 ($V_{HW}/V_{FW} = 1.7$; Figs. 12B and 12C), which could indicate the position of a through-going input point. This position coincides with the highest measured headward and vertical erosion along the fault. The fan in Q6 shows clinoforms in Unit Set 1 and slope apron geometries in Unit Sets 2-3 (position VI, Fig. 11). A second major positive peak occurs in Q7 ($V_{HW}/V_{FW} = 1.5$; Figs. 12B and 12C). This is coincident with highs in vertical and headward erosion, a fault throw minimum (Fig. 12A), and a topographic high in the hangingwall basin (Fig. 9). This peak also occurs where sustained clinoform development is apparent throughout Unit Sets 1-3, with clinoforms defined by clear topsets and radial foresets (SF1b, Table 1; position VII, Fig. 11). Another peak, in Q3 ($V_{HW}/V_{FW} = 1.6$; Fig. 12B) coincides with clinoform development in the hangingwall in Unit Sets 1-2 (Fig. 13). This peak does not correlate with peaks in headward and vertical erosion, but such highs occur in the adjacent Q2. One hypothesis may be that fans prograded obliquely

from Q2 to Q3, an interpretation that is supported by the fan in Unit E being skewed towards the NE (Top Unit E contour map, Fig. 11A).

As previously discussed, our volume balancing approach underestimates hangingwall cell volume compared to footwall cell volume by up to 15%. This means any ratio value is a minimum estimate. As such, it is possible that areas characterised by excess erosion ($V_{HW}/V_{FW} < 1$) may be closer to a balance, and areas characterised by excess hangingwall-fill ($V_{HW}/V_{FW} > 1$) are underestimated. This supports our interpretation that Q3, Q6 and Q7 were defined by through-going sediment dispersal systems.

7. Tectono-stratigraphic evolution

7.1. Phase 1 – Unit Set 1

Thickening of Unit Set 1 strata into the main border fault suggests that the fault became active at this time (Fig. 13). Small, footwall-derived fan deltas began to build at discrete locations along the main border fault, as evidenced by the development of clinoforms. Small foreset heights in Unit Set 1 suggests relatively shallow water depths at this time. The progradational stacking of fans towards the north-eastern fault tip (Q3, Fig. 13) suggests that sediment supply outpaced accommodation creation in the hangingwall. Conversely, aggradational stacking towards the fault centre (Q6, Fig. 13) implies that sediment supply and accommodation creation were approximately equivalent. For a given sediment supply, this stacking distribution is typical of hangingwall basins where fault-related subsidence presents a parabolic distribution along-strike, with maximum subsidence towards the fault centre and minima at the fault tips (Walsh & Watterson, 1988; Gawthorpe et al., 1994; 2003; Dawers & Anderson, 1995; Hardy & Gawthorpe, 1998; Hunt & Gawthorpe, 2000; Childs et al., 2003; Jackson et al., 2005; Serck & Braathen, 2019). In Q7, the fan delta presents a progradational geometry despite being relatively close to the fault centre, either suggesting enhanced sediment supply and/or reduced accommodation creation at this position. The fan delta is positioned at a structural high defining the boundary between the central and southern sub-basins. Here, a fault throw minima is interpreted as a breached relay, indicating low rates of subsidence and accommodation creation during the early stages of fault development. Sediment input may also have been focussed through the relay zone at this time (Gawthorpe & Hurst, 1993; Leeder & Jackson, 1993; Gupta et al., 1999; Densmore et al., 2003; Fossen & Rotevatn, 2016). This sediment input then became fixed in the landscape and continued to supply sediment throughout the basin evolution.

7.2. Phase 2 – Unit Set 2

Unit Set 2 strata dip and start to thicken towards antithetic faults AB and AC, which suggests that these faults became active at this time (Fig. 13). Footwall-derived fans continued to aggrade in the immediate

hangingwall of the main border fault, but their geometry changed. For example, the earlier (Unit Set 1) fan delta in Q6 was overlain by slope apron deposits (SF1a, Table 1); this implies basin deepening, which is likely a result of increased fault-related subsidence. In the northern sub-basin (Q3) and at the structural high between the central and southern sub-basins (Q7), two fan deltas continued to build, suggesting reduced subsidence and accommodation creation, or enhanced sediment supply at these specific locations. Fan delta stacking patterns in Q7 changed from progradational to aggradational-retrogradational at this time, suggesting reduced sediment supply or enhanced accommodation creation relative to that characterising Phase 1. Hangingwall-derived, submarine fans prograded from antithetic faults AB and AC, and interfingered at their distal margin with footwall-derived fans from the main border fault (Fig. 13). The fault scarp was subaerially exposed at this time, facilitating degradation, which was greatest at the fault centre and least at the fault tips. This pattern of erosion reflects the present distribution of slip and throw on the basin-bounding fault. Antithetic fault crests lack seismic-scale erosion and are interpreted to be submerged.

7.3. Phase 3 – Unit Set 3

Fault-scarp degradation along the main border fault continued, feeding hangingwall slope aprons and submarine fans (Fig. 13). The through-going, fixed sediment input persisted in Q7, as the fan delta underwent a period of progradation before retrogradation. Progradation could reflect an increased sediment supply, reduced activity on the fault (and thus accommodation creation), or a relative base level fall. An eventual return to the general retrogradational trend characterising other along-strike locations likely reflects an increase in fault-related subsidence. Strata thicken into antithetic faults AA and AD at this time, implying they had become active. At the structural high between the central and southern sub-basins, a hangingwall-derived fan delta prograded from antithetic fault AD, towards the SE. The fan delta downlapped onto and prograded up the distal margin of the footwall-derived fan delta in Q7, prograding towards the NW (Fig. 13). During this phase, the footwall-derived fan delta in Q3 was drowned and became a slope apron. Axial drainage from near the northern fault tip, parallel to the fault, then dominated sediment dispersal. Strongly progradational clinoforms suggest a deltaic origin with a high sediment supply. These deltas prograded around topography related to preceding and concurrent footwall-derived deposits (Fig. 10D). Two sets of stacked foresets are observed, separated by flat-lying reflections that are tentatively interpreted to represent flooding surfaces formed during two minor relative sea level cycles (Fig. 10E).

7.4. Phase 4 – Unit Set 4

Footwall-derived slope apron deposits continued to be locally deposited during Phase 4 (Fig. 13). An exception occurs at Q6, where a large submarine fan formed, basinward of the area of greatest footwall degradation. The absence of clinoforms suggests that the fan delta in Q7 was drowned. Elsewhere, lower angle dips and multiple onlaps in various directions indicate passive infilling of the basin, most

likely be pelagic or hemipelagic sediment. The depositional environment at this time is unclear, but given the absence of clinoformal geometries that are otherwise indicative of a marginal setting, and the presence of suspected subaqueous fans against the main border fault, it is speculated to be a deeper water basin than in Phases 1-3. The lack of thickness changes across the antithetic faults suggest they were no longer active; the basin-bounding faults may also have become inactive at this time.

8. Discussion

Through analysis of footwall erosion and hangingwall-fill, we have identified the positions of through-going sediment input points and have some constraint of the catchment history from the fault footwall. Moreover, we have assessed the contribution of sediment sources from other positions in the basin (hangingwall- and axial-derived), and the along-strike variability of their deposits through time. Here, we discuss the implications of these outcomes for: 1) footwall catchment identification in rifts and, 2) sediment supply to rift basins.

8.1. Where are the footwall catchments?

We undertook a novel, volume balancing approach to identify whether sediment was sourced solely from footwall degradation, or whether intra-basin catchments were also important. We found excess hangingwall-fill ($V_{HW} > V_{FW}$), which suggests that fault scarp degradation was not the only sediment source. Using the ratio and difference between the two (V_{HW}/V_{FW} and $V_{HW}-V_{FW}$) for geometrically defined quadrants along the fault, we could more precisely constrain the areas that were dominated by sediment bypass ($V_{HW} < V_{FW}$) and the areas that coincide with fixed, through-going sediment input points ($V_{HW} > V_{FW}$).

Excess hangingwall-fill was highlighted in Q3, 6 and 7, as the positions of through-going sediment input points and thus, catchments beyond the fault crest. Q7 coincides with the topographic high between the central and southern sub-basins, a fault throw minima, peaks in vertical and headward erosion, and sustained clinoform development in the immediate hangingwall through Phases 1-3. It is interpreted that sediments entered the basin here through a relay zone (Phase 1) that was later breached, yet continued be a focal basin entry point (Phase 2-3) (e.g. Young et al., 2003). In Q3 and 6, early clinoforms in the hangingwall were overlain by slope apron deposits. Q6 is characterised by the highest headward and vertical erosion. Q3 is suggested to be fed obliquely by high erosion in Q2. It was not possible to constrain the timing of erosion relative to hangingwall sedimentation from the volume-balancing approach alone. Seismic mapping of clinoforms and planar-sloping reflectors in the hangingwall stratigraphy can resolve deltaic versus slope apron deposits, and formed the basis of the relative timing interpretation (Fig. 13). Our interpretations suggest that through-going sediment inputs switched off (sediment supply reduced) in various phases (Fig. 13), which could have resulted from

18

slope changes associated to fault growth (e.g. Cowie et al., 2006; Attal et al., 2008). It is also possible that the transition from fan delta to slope apron deposits in the hangingwall did not occur from the switching-off of sediment inputs, but was the result of subsidence rate increasing and outpacing the sediment supply.

The Thebe sub-basin was (and still is) located in a relatively distal position on the northern Carnarvon basin. Regional stratigraphic analysis reports an overall increase in water depth from the Late Triassic to the Late Jurassic (J40) (Hocking et al., 1988; Longley et al., 2002; Marshall & Lang, 2013). Although we have no constraints on the precise timing of the basin fill, our volume balancing approach, and observations of fault-scarp degradation and hangingwall clinoform development suggests: 1) a relatively shallow water environment, 2) exposure of the footwall crest, and 3) the presence of palaeo-coastlines against the main border fault during Phases 1-3, and against antithetic fault AD during Phase 3. In Phase 4, these sources were flooded as sea-level rose. Bilal et al. (2018) argue that adjacent footwall scarps in the northern Carnarvon Basin were degraded in a subaqueous environment, based on the absence of submarine canyon development and subaerial indicators in well data. However, the authors did not provide a mechanistic explanation for clinoform development and footwall crest degradation of this scale, and fixed through-going input points, in a fully marine setting, in the absence of a subaerial source. Our interpretation is consistent with large-scale, palaeogeographic maps from the J30 sequence (Longley et al., 2002) that show deposition in narrow rift valleys and palaeo-coastlines fringing exposed fault blocks. Similar scenarios of uplifted and exposed footwall highs and islands supplying hangingwall basins are interpreted in the Late Jurassic North Sea (Yielding et al., 1992; Berger & Roberts, 1999; Nøttvedt et al., 2000; McArthur et al., 2016b; Roberts et al., 2019) and the Quaternary-modern Aegean Sea (Papadopoulos & Palvides, 1992; Stiros et al., 1994).

8.2. Sediment supply in rift basins

The volume of sediment in Units E and H amounts to ~10% of the total hangingwall-fill. Footwall-derived material is apparent in other units, so this is a minimum estimate of footwall-derived material in the hangingwall basin. However, the hangingwall- and axial-derived systems (and pelagic and hemipelagic material) made a clear and substantial contribution to the basin-fill (~90%), and their relative influence changed through time as the basin evolved. In the early stages of the basin, footwall-derived systems were most prominent, likely because of border fault activity. Later, footwall-derived systems continued to build, but changed in style along-strike according to the local ratio of accommodation creation to sediment supply. Hangingwall-derived systems started to play an important role when antithetic faults became active. Subsequently, the axial system, which prograded from the northern fault tip, established itself and formed a large component of Unit G. No system prograded axially from the southern fault tip. The growth and interaction of adjacent faults outside of the

immediate study area and local antithetic faults generated variable intra-basin relief and gradients, and are thus likely to have played a role in determining sediment flux, entry points, and the migration of depositional systems around the basin (Gawthorpe & Hurst, 1993; Roberts et al., 1993; Ravnås & Steel, 1998; Whittaker et al., 2010).

Coeval and competing sediment supply systems result in complex process and architectural interactions and should be an important aspect of tectono-sedimentary models for rifts. Here, depositional systems represent a spectrum of compensational stacking styles (e.g. Mohrig et al., 2000; Olariu & Bhattacharya, 2006; Prélat et al., 2009; Wang et al., 2011; Straub & Pyles, 2012; Bell et al., 2018), and are observed to interfinger, abruptly downlap, to build up the flanks of another, or to route around each other. The relative timing of establishment and progradation of different depositional systems clearly plays an important role in this interaction, but also the depositional gradients of the competing systems (Dodd et al., 2018) and the individual stream power of, for example river systems, given it is this which strongly influences its ability to erode and/or bypass (Stevenson et al., 2015). However, we note that the widely used conceptual models for the tectono-sedimentary evolution of rifts do not capture interacting sediment supply systems of different origins and stacking patterns, and instead emphasise footwall-derived depositional systems (e.g. Gawthorpe & Leeder, 2000). This is in part due to the prolificacy of the rift basins that have been studied to generate these models; the Gulf of Corinth has been particularly influential in this regard, as it is characterised by a number of large, antecedent, transverse drainage systems that are excellently exposed (Dart et al., 1994; Gawthorpe et al., 1994; Ford et al., 2007; Rohais et al., 2007; Backert et al., 2010; Gobo et al., 2015; Barrett et al., 2019a,b). These models need to be adapted to incorporate contribution and interactions of other sediment entry points to the basin that this and other recent studies have highlighted (e.g. McArthur et al., 2016a; Henstra et al., 2017; Muravchik et al., 2018; Cullen et al., 2019).

8.3. Implications for hydrocarbon exploration

We have documented the styles of interaction between footwall-, hangingwall- and axial-derived depositional systems and these are important when assessing petroleum systems development in rifts. For example, it can ultimately define the distribution, connectivity, trapping, and pinch-out geometries associated with their related reservoirs. Our quantitative volumetric approach could be applied to identify the position of through-going sediment input points in other hydrocarbon-bearing rifts. These far-field sources yield sediment that has travelled further, and are is thus likely to be more reworked and mature than sediment derived from the immediately adjacent fault scarp (Reading & Richards, 1994; Richards et al., 1998; Leppard & Gawthorpe, 2006). Therefore, when prospecting hangingwall fans, areas sourced by established catchments beyond the footwall crest could have higher reservoir quality and thus deliverability. Our approach could be similarly used to identify areas dominated by

sediment bypass (Stevenson et al., 2015); it could thus be a useful tool in the search for prospective subaqueous fans deposited further basinward, perhaps in the basin axis. Both approaches would ideally be performed with depth-converted seismic reflection data build from a well-constrained velocity model; this would allow for a more accurate estimate of eroded and deposited sediment volumes. However, as we demonstrate, it is still possible to estimate and work with the volume balance ratio derived from time-migrated seismic reflection data. Identification and mapping of footwall catchments and/or imaging of footwall-derived, hangingwall clinoforms supports our volume balancing approach. Here, footwall catchments beyond the fault crest were not imaged, but mapping hangingwall clinoforms was possible. In areas where data quality restricts the imaging of footwall catchments or hangingwall clinoforms, this approach could be used.

9. Conclusion

A quantitatively-informed interpretation of the tectono-sedimentary evolution of an individual fault block in the northern Carnarvon Basin, NW Shelf, offshore Australia, suggests that the basin evolved through four phases linked to the evolution of the main border fault and a number of parallel, antithetic faults, which became active at different times. Through-going sediment input points were identified in Quadrants 3, 6 and 7. The latter persisted throughout the basin evolution and coincides with the saddle (topographic high) between the central and southern sub-basins, a fault throw minimum, peaks in vertical and headward erosion, and convincing and sustained clinoform development in the immediate hangingwall. Exposure of the border fault footwall and inboard/adjacent fault terraces (that may have become active earlier) are interpreted to have produced small catchments that fed the hangingwall basin, reflecting deposition in narrow rift valleys and palaeo-shorelines that fringed emergent fault blocks in the outboard part of the northern Carnarvon Basin.

Overall there are two main outcomes of this study that represent advances in the fields of syn-rift geomorphology and tectono-stratigraphy:

1) Complex process and architectural interactions are observed between depositional systems within the same basin, but with different origins (footwall-, hangingwall- and axial-derived) that yield similar contributions to the hangingwall-fill. Depositional systems are observed to interfinger, abruptly downlap, build up the flanks of another, or route around each other, which represents a spectrum of compensational stacking styles within a fault-confined basin. This is an important outcome which should be incorporated into existing models for tectono-sedimentary development in rift basins.

2) A quantitative approach is presented that could be used to independently locate through-going input points in other basins, particularly where preservation of erosional landscapes are limited and/or

subsurface imaging is challenging. Similarly, it could be useful tool for identifying areas along a fault that were dominated by sediment bypass.

10. Acknowledgements

11. References

Attal, M., Tucker, G.E., Whittaker, A.C., Cowie, P.A. & Roberts, G.P. (2008). Modeling fluvial incision and transient landscape evolution: influence of dynamic channel adjustment. *Journal of Geophysical Research*, 113, F03013, doi: 10.1029/2007JF000893.

Backert, N., Ford, M. & Malartre, F. (2010). Architecture and sedimentology of the Kerinitis Gilbert-type fan delta, Corinth Rift, Greece. *Sedimentology*, 57, 543-586.

Barrett, B.J., Collier, R.E.Ll., Hodgson, D.M., Gawthorpe, R.L., Dorrell, R.M. & Cullen, T.M. (2019a). Quantifying faulting and base level controls on syn-rift sedimentation using stratigraphic architectures of coeval, adjacent Early-Middle Pleistocene fan deltas in Lake Corinth, Greece. *Basin Research*, doi: 10.1111/bre.12356.

Barrett, B.J., Gawthorpe, R.L., Collier, R.E.Ll., Hodgson, D.M. & Cullen, T.M. (2019b). Syn-rift deltaic interfan stratigraphy as archives of sedimentation and basin evolution. *The Depositional Record*, 6, 117-143.

Barrett, B.J., Hodgson, D.M., Collier, R.E.Ll. & Dorrell, R.M. (2018). Novel 3D sequence stratigraphic numerical model for syn-rift basins: analysing architectural responses to eustasy, sedimentation and tectonics. *Marine and Petroleum Geology*, 92, 270-284.

Bell, D., Stevenson, C., Kane, I., Hodgson, D.M. & Poyatos-Moré, M. (2018). Topographic controls on the development of contemporaneous but contrasting basin-floor depositional architectures. *Journal of Sedimentary Research*, 88, 1169-1189.

Berger, M. & Roberts, M. (1999). The Zeta Structure: a footwall degradation complex formed by gravity sliding on the western margin of the Tampen Spur, Northern North Sea. *Geological Society, London, Petroleum Geology Conference series*, 5, 107-116.

Bilal, A., McClay, K. & Scarselli, N. (2018). Fault-scarp degradation in the central Exmouth Plateau North West Shelf, Australia. In: K.R. McClay & J.A. Hammerstein (Eds.), *Passive margins: tectonics, sedimentation and magmatism.* Geological Society, London, Special Publications, 476, doi: 10.1144/SP476.11.

Bradshaw, M.T., Bradshaw, J., Murray, A.P., Needham, D.J., Spencer, L., Summons, R.E., Wilmot, J. & Winn, S. (1994). Petroleum systems in west Australian basins. In: P.G. Purcell & R.R. Purcell (Eds.), *The Sedimentary Basins of Western Australia: Proceedings of the Petroleum Exploration Society of Australia Symposium.* PESA, Perth, 93-118.

Bradshaw, M.T., Yeates, A.N., Beynon, R.M., Brakel, A.T., Langford, R.P., Totterdell, J.M. & Yeung, M. (1988). Palaeogeographic evolution of the North West Shelf region. In: P.G. Purcell & R.R. Purcell (Eds.), *Proceedings of the North West Shelf Symposium.* PESA, Perth, 29-54.

Childs, C., Nicol, A., Walsh, J.J. & Watterson, J. (2003). The growth and propagation of synsedimentary faults. *Journal of Structural Geology*, 25, 633-648.

Collier, R.E.Ll. & Gawthorpe, R.L. (1995). Neotectonics, drainage and sedimentation in central Greece: insights into coastal reservoir geometries in syn-rift sequences. *Geological Society, London, Special Publications*, 80, 165-181.

Cowie, P.A., Attal, M., Tucker, G.E., Whittaker, A.C., Naylor, M., Ganas, A. & Roberts, G.P. (2006). Investigating the surface process response to fault interaction and linkage using a numerical modelling approach. *Basin Research*, 18, 231-266.

Cowie, P.A., Gupta, S. & Dawers, N.H. (2000). Implications of fault array evolution for synrift depocenter development: insights from a numerical fault growth model. *Basin Research*, 12, 241-261.

Crameri, F. (2018). Scientific colour-maps. Zenodo. doi: 10.5281/zenodo.1243862.

Cullen, T.M., Collier, R.E.Ll., Gawthorpe, R.L., Hodgson, D.M. & Barrett, B.J. (2019). Axial and transverse deep-water sediment supply to syn-rift fault terraces: insights from the West Xylokastro Fault Block, Gulf of Corinth, Greece. Basin Research, doi; 10.1111/bre.12416.

Dart, C.J., Collier, R.E.Ll., Gawthorpe, R.L., Keller, J.V.A. & Nichols, G. (1994) Sequence stratigraphy of (?)Pliocene-quaternary synrift, gilbert-type fan deltas, Northern Peloponnesos, Greece. *Marine and Petroleum Geology,* 11, 545-560.

Dawers, N. H. & Anderson, M.H. (1995). Displacement-length scaling and fault linkage. *J. Struct. Geol.,* 17, 607-614.

Densmore, A.L., Dawers, N.H., Gupta, S., Allen, P.A. & Gilpin, R. (2003). Landscape evolution at extensional relay zones. *Journal of Geophysical Research*, 108, doi:10.1029/2001JB001741.

Dodd, T.J., McCarthy, D.J. & Richards, P.C. (2018). A depositional model for deep-lacustrine, partially-confined, turbidite fans: Early Cretaceous, North Falkland Basin. *Sedimentology*, 66, 53-80.

Dorsey, R.J. & Umhoefer, P.J. (2000). Tectonic and eustatic controls on sequence stratigraphy of the Pliocene Loreto Basin, Baja California Sur, Mexico. *GSA Bulletin*, 112, 177-199.

Dorsey, R.J., Umhoefer, P.J. & Renne, P.R. (1995). Rapid subsidence and stacked gilbert-type fan deltas, Pliocene Loreto Basin, Baja California Sur, Mexico. *Sedimentary Geology*, 98, 181-204.

Elliott, G.M., Wilson, P., Jackson, C.A.-L., Gawthorpe, R.L., Michelsen, L. & Sharp, I. (2012). The linkage between fault throw and footwall scarp erosion patterns: an example from the Bremstein Fault Complex, offshore Mid-Norway. *Basin Research*, 24, 180-197.

Ellis, C., Woodall, M., Goody, A., Lim, D. & Locke, M. (2009). Thebe-2 and Thebe-2CH well completion report, interpretive volume, WA-346-P. BHP Billiton Petroleum Pty Ltd.

Etheridge, M.A. & O'Brien, G.W. (1994). Structural and tectonic evolution of the Western Australia margin system. *PESA Journal*, 22, 45-63.

Evans, A.L. (1990). Miocene sandstone provenance relations in the Gulf of Suez: insights into synrift unroofing and uplift history. *AAPG Bulletin*, 9, 1386-1400.

Exon, N.F., Haq, B.U. & von Rad, U. (1992). Exmouth Plateau revisited: scientific drilling and geological framework. *Proceedings of the Ocean Drilling Program, Scientific Results,* 122, 3-20.

Ford, M., Williams, E.A., Malartre, F. & Popescu, S.M. (2007). Stratigraphic architecture, sedimentology and structure of the Vouraikos Gilbert-type fan delta, Gulf of Corinth, Greece. In: G. Nichols, E. Williams & C. Paola (Eds.), *Sedimentary Processes, Environments and Basins. A Tribute to Peter Friend*. Int. Assoc. Sedimentol. Spec. Publ., 38, 49-90.

Forman, D.J. & Wales, D.W. (1981). Geological evolution of the Canning Basin, Western Australia. *Bureau of Mineral Resources, Geology and Geophysics Bulletin*, 210, 91pp.

Fossen, H. & Rotevatn, A. (2016). Fault linkage and relay structures in extensional settings − a review. *Earth-Science Reviews*, 154, 14-28.

Fraser, S.I., Robinson, A.M. et al. (2002). Upper Jurassic. In: A. Armour, D. Evans & C. Hickey (Eds.), *The Millenium Atlas: Petroleum Geology of the Central and Northern North Sea*. The Geological Society, London, 157-189.

Gartrell, A., Torres, J., Dixon, M. & Keep, M. (2016). Mesozoic rift onset and its impact on the sequence stratigraphic architecture of the Northern Carnarvon Basin. *The APPEA Journal*, 56, 143-158.

Gawthorpe, R. L., Andrews, J. E., Collier, R. E. Ll., Ford, M., Henstra, G.A., Kranis, H., Leeder, M.R., Muravchik, M. & Skourtsos, E. (2017). Building up or out? Disparate sequence architectures along an active rift margin – Corinth rift, Greece. *Geology*, 45, 111-114.

Gawthorpe, R. L., Fraser, A.J. & Collier, R.E.Ll. (1994). Sequence stratigraphy in active extensional basins: implications for the interpretation of ancient basin-fills. *Marine and Petroleum Geology*, 11, 642-658.

Gawthorpe, R.L., Hardy, S. & Ritchie, B. (2003). Numerical modelling of depositional sequences in halfgraben rift basins. *Sedimentology*, 50, 169-185.

Gawthorpe, R. L. & Hurst, J.M. (1993). Transfer zones in extensional basins: their structural style and influence on drainage development and stratigraphy. *Journal of the Geological Society, London*, 150, 1137-1152.

Gawthorpe, R.L. & Leeder, M.R. (2000). Tectono-sedimentary evolution of active extensional basins. *Basin Research*, 12, 195-218.

Ghinassi, M. (2007). The effects of differential subsidence and coastal topography on high-order transgressive-regressive cycles: Pliocene nearshore deposits of the Val d'Orcia Basin, Northern Apennines, Italy. *Sedimentary Geology*, 202, 677-701.

Gobo, K., Ghinassi, M. & Nemec, W. (2015). Gilbert-type deltas recording short-term base-level changes: delta-brink morphodynamics and related foreset facies. *Sedimentology*, 62, 1923-1949.

Gupta, S., J. R. Underhill, I. R. Sharp, & R. L. Gawthorpe (1999). Role of fault interaction in controlling synrift dispersal patterns: Miocene, Abu Alaqa Group, Suez Rift, Sinai, Egypt. *Basin Research*, 11, 167-189.

Hampson, G.J., Duller, R.A., Petter, A.L., Robinson, R.A.J. & Allen, P.A. (2014). Mass-balance constraints on stratigraphic interpretation of linked alluvial-coastal-shelfal deposits from source to sink: example from Cretaceous Western Interior Basin, Utah and Colorado, USA. *Journal of Sedimentary Research*, 84, 935-960.

Hardy, S. & Gawthorpe, R.L. (1998). Effects of variations in fault slip rate on sequence stratigraphy in fan deltas: insights from numerical modeling. *Geology,* 26, 911-914.

Hartley, R.A., Roberts, G.G., White, N. & Richardson, C. (2011). Transient convective uplift of an ancient buried landscape. *Nature Geoscience*, 4, 562-565.

Hengesh, J.V. & Whitney, B.B. (2016). Transcurrent reactivation of Australia's western passive margin: an example of intraplate deformation from the central Indo-Australian plate. *Tectonics*, 35, 1066-1089.

Henstra, G.A., Grundvåg, S-A., Johannessen, E.P., Kristensen, T.B., Midtkandal, I., Nystuen, J.P., Rotevatn, A., Surlyke, F., Sætherf, T. & Windelstad, J. (2016). Depositional processes and stratigraphic architecture within a coarse-grained rift-margin turbidite system: The Wollaston Forland Group, East Greenland. *Marine and Petroleum Geology*, 76, 187-209.

Henstra, G.A., Gawthorpe, R.L., Helland-Hansen, W., Ravnås, R. & Rotevatn, A. (2017). Depositional systems in multiphase rifts: seismic case study from the Lofoten margin, Norway. *Basin Research*, 29, 447-469.

Hocking, R.M. (1988). Regional Geology of the Northern Carnarvon Basin. In: P.G. Purcell and R.R. Purcell (Eds.), *The North West Shelf, Australia. Proceedings of Petroleum Exploration Society of Australia Symposium*. PESA, Perth, 97-114.

Hunt, D. & Gawthorpe, R.L. (2000). Sedimentary responses to forced regressions. *Geological Society, London, Special Publications*, 172.

Jackson, C.A.-L., Bell, R.E., Rotevatn, A., Tvedt, A.B.M. (2017). Techniques to determine the kinematics of syn-sedimentary normal faults and implications for fault growth models. In: C. Childs, R.E. Goldsworth, C.A.-L. Jackson, T. Manzocchi, J.J. Walsh & G. Yielding (Eds.), *The Geometry and Growth of Normal Faults*. Geological Society, London, Special Publications, 439, 187-217.

Jackson, C.A.-L., Gawthorpe, R.L., Carr, I.D. & Sharp, I.R. (2005). Normal faulting as a control on the stratigraphic development of shallow marine syn-rift sequences: the Nukhul and Lower Rudeis Formations, Hammam Faraun fault block, Suez Rift, Egypt. *Sedimentology,* 52, 313-338.

Jackson, C.A.-L., Gawthorpe, R.L., Sharp, I.R. (2006). Style and sequence of deformation during extensional fault-propagation folding: examples from the Hammam Faraun and El-Qaa fault blocks, Suez Rift, Egypt. *Basin Research*, 28, 519-535.

Jackson, C.A.-L., Larsen, E., Hanslien, S. & Tjemsland, A.-E. (2011). Controls on synrift turbidite deposition on the hanging wall of the South Viking Graben, North Sea rift system, offshore Norway. *AAPG Bulletin*, 95, 1557-1587.

Jackson, J. A. & Leeder, M.R. (1993). Drainage systems and the evolution of normal faults: an example from Pleasant Valley, Nevada. *Journal of Structural Geology*, 16, 1041-1059.

Kallweit, R.S. & Wood, L.C. (1982). The limits of resolution of zero-phase wavelets. *Geophysics*, 47, 1035-1046.

Keep, M., Powell, C.M. & Baillie, P.W. (1998). Neogene deformation of the North West Shelf, Australia. In: P.G. Purcell & R.R. Purcell (Eds.), *The Sedimentary Basins of Western Australia 2: Proceedings of Petroleum Exploration Society Australia Symposium*. PESA, Perth, 81-91.

Leeder, M. R., & J. A. Jackson (1993), The interaction between normal faulting and drainage in active extensional basins, with examples from the western United States and central Greece. *Basin Research*, 5, 79-102.

Leeder, M.R., Mack, G.H. & Salyards, S.L. (1996). Axial-transverse fluvial interactions in half graben: Plio-Pleistocene Palomas Basin, southern Rio Grande Rift, New Mexico, USA. *Basin Research*, 8, 225-241.

Leppard, C.W. & Gawthorpe, R.L. (2006). Sedimentology of rift climax deep water systems; Lower Rudeis Formation, Hammam Faraun Fault Block, Suez Rift, Egypt. *Sedimentary Geology*, 191, 67-87.

Lewis, M.M., Jackson, C.A.-L. & Gawthorpe, R.L. (2015). Tectono-sedimentary development of early syn-rift deposits: the Abura Graben, Suez Rift. *Basin Research*, 29, 327-351.

Lin, W. & Bhattacharya, J.P. (2017). Estimation of source-to-sink mass balance by a fulcrum approach using channel paleohydrologic parameters of the Cretaceous Dunvegan Formation, Canada. *Journal of Sedimentary Research*, 87, 97-116.

Longley, I.M., Buessenschuett, C., Clydsdale, L., Cubitt, C.J., Davis, R.C., Johnson, M.K., Marshall, N.G., Murray, A.P., Somerville, R., Spry, T.B. & Thompson, N.B. (2002). The North West Shelf of Australia – a Woodside perspective. In: M. Keep & S.J. Moss (Eds.), *The Sedimentary Basins of Western Australia 3: Proceedings of the Petroleum Society of Australia Symposium*. PESA, Perth, 966pp.

Marshall, N.G. & Lang, S.C. (2013). A New Sequence Stratigraphic Framework for the North West Shelf, Australia. In: M. Keep & S.J. Moss (Eds.), *The Sedimentary Basins of Western Australia 4: Proceedings of Petroleum Exploration Society of Australia Symposium*. PESA, Perth, 18-21.

McArthur, A.D., Hartley, A.J., Archer, S.G., Jolley, D.W. & Lawrence, H.M. (2016a). Spatiotemporal relationships of deep-marine, axial, and transverse depositional systems from the synrift Upper Jurassic of the central North Sea. *AAPG Bulletin*, 100, 1469-1500.

McArthur, A.D., Jolley, D.W., Hartley, A.J., Archer, S.G. & Lawrence, H.M. (2016b). Palaeoecology of syn-rift topography: a Late Jurassic footwall island on the Josephine Ridge, Central Graben, North Sea. *Palaeogeography, Palaeoclimatology, Palaeoecology*, 459, 63-75.

McLeod, A.E. & Underhill, J.R. (1999). Processes and products of footwall degradation, northern Brent Field, Northern North Sea. Geological Society, London, Petroleum Geology Conference series, 5, 91-106.

Metcalfe, I. (1999). Gondwana dispersion and Asian accretion: An overview. In: I. Metcalfe (Ed.), *Gondwana Dispersion and Asian Accretion – IGCP 321 Final Results Volume*. A.A. Balkema, Rotterdam, 9-28.

Michael, N.A., Whittaker, A.C. & Allen, P.A. (2013). The functioning of sediment routing systems using a mass balance approach: example from the Eocene of the Southern Pyrenees. *The Journal of Geology*, 121, 581-606.

Mohrig, D., Heller, P.L., Paola, C.& Lyons, W.J. (2000). Interpreting avulsion process from ancient alluvial sequences: Guadalope-Matarranya (northern Spain) and Wasatch Formation (western Colorado). *Geological Society of America Bulletin,* 112, 1787-1803.

Morley, C.K., Ionnikoff, Y., Pinyochon, N. & Seusutthiya, K. (2007). Degradation of a footwall fault block with hanging-wall fault propagation in a continentallacustrine setting: how a new structural model impacted field development plans, the Sirikit field, Thailand. *AAPG Bulletin*, 91, 1637-1661.

Mortimer, E.J. & Carrapa, B. (2007). Footwall drainage evolution and scarp retreat in response to increasing fault displacement: Loreto fault, Baja California Sur, Mexico. *Geology*, 35, 651-654.

Muravchik, M., Gawthorpe, R.L., Sharp, I.R., Rarity, F. & Hodgetts, D. (2018). Sedimentary environment evolution in a marine hangingwall dipslope setting. El Qaa Fault Block, Suez Rift, Egypt. *Basin Research*, 30, 452-478.

Nøttvedt, A, Berge, A.M., Dawers, N.H., Færseth, R.B., Häger, K.O., Mangerud, G. & Puigdefabregas, C. (2000). Syn-rift evolution and resulting play models in the Snorre-H area, northern North Sea. In: A. Nøttvedt (Ed.), *Dynamics of the Norwegian Margin*. Geological Society, London, Special Publications, 167, 179-218.

Olariu, C. & Bhattacharya, J.P. (2006). Terminal distributary channels and delta front architecture of river-dominated delta systems. *Journal of Sedimentary Research,* 76, 212-233.

Paola, C. & Martin, J.M. (2012). Mass-balance effects in depositional systems. *Journal of Sedimentary Research*, 82, 435-450.

Papadopoulos, G. & Pavlides, S. (1992). The large 1956 earthquake in the South Aegean: macroseismic field configuration, faulting and neotectonics of Amorgos Island. *Earth Planet. Sci. Letters*, 113, 383-396.

Pechlivanidou, S., Cowie, P.A., Hannisdal, B., Whittaker, A.C., Gawthorpe, R.L., Pennos, C. & Riiser, O.S. (2018). Source-to-sink analysis in an active extensional setting: Holocene erosion and deposition in the Sperchios rift, central Greece. *Basin Research*, 30, 522-543.

Phillips, T.B., Jackson, C. A. L., Bell, R. E. & Duffy, O. B. (2018). Oblique reactivation of lithosphere-scale lineaments controls rift physiography – the upper-crustal expression of the Sorgenfre-Tornquist Zone, offshore southern Norway. *Solid Earth*, 9, 403-429.

Prélat, A., Hodgson, D.M. & Flint, S.S. (2009). Evolution, architecture and hierarchy of distributary deep-water deposits: a high-resolution outcrop investigation from the Permian Karoo Basin, South Africa. *Sedimentology*, 56, 2132-2154.

Ravnås, R. & Steel, R.J. (1998). Architecture of Marine Rift-Basin Successions. *AAPG Bulletin*, 82, 110-146.

Reading, H.G. & Richards, M. (1994). Turbidite systems in deep-water basin margins classified by grain size and feeder system. *AAPG Bulletin*, 78, 792-822.

Richards, M., Bowman, M. & Reading, H. (1998). Submarine fan systems characterization and stratigraphic prediction. *Marine and Petroleum Geology*, 15, 689-717.

Roberts, A.M., Kusznir, N.J., Yielding, G. & Beeley, H. (2019). Mapping the bathymetric evolution of the Northern North Sea: from Jurassic synrift archipelago through Cretaceous-Tertiary post-rift subsidence. Petroleum Geoscience, 25, 306-321.

Roberts, A. M., Yielding, G. & Badley, M.E. (1993). Tectonic and bathymetric controls on stratigraphic sequences within evolving half-graben. In: G. D. Wouldiams & A. Dobb (Eds.), *Tectonics and seismic sequence stratigraphy*. Geological Society Special Publication, 71, 87-121.

Rohais, S., Eschard, R., Ford, M., Guillocheau, F. & Moretti, I. (2007). Stratigraphic architecture of the Plio-Pleistocene infill of the Corinth Rift: implications for its structural evolution. *Tectonophysics*, 440, 5-28.

Serck, C.S. & Braathen, A. (2019). Extensional fault and fold growth: impact on accommodation evolution and sedimentary infill. *Basin Research*, doi: 10.1111/bre.12353.

Sharp, I.R., Gawthorpe, R.L., Armstrong, B. & Underhill, J.R. (2000). Propagation history and passive rotation of mesoscale normal faults: implications for synrift stratigraphic development. *Basin Research*, 12, 285-305.

Sharp, I.R., Gawthorpe, R.L., Underhill, J.R. & Gupta, S. (2000). Fault-propagation folding in extensional settings: examples of structural style and synrift sedimentary response from the Suez rift, Sinai, Egypt. *Geological Society of America Bulletin*, 112, 1877-1899.

Smallwood, J.R. & Gill, C.E. (2002). The rise and fall of the Faroe-Shetland Basin: Evidence from seismic mapping of the Balder Formation. Journal of the Geological Society, 159, 627-630.

Stagg, H.M.J. & Colwell, J.B. (1994). The structural foundations of the Northern Carnarvon Basin. In: P.G. Purcell & R.R. Purcell (Eds.), *The North West Shelf, Australia. Proceedings of Petroleum Exploration Society of Australia Symposium*. PESA, Perth, 349-372.

Stevenson, C.J., Jackson, C.A.-L., Hodgson, D.M., Hubbard, S.M. & Eggenhuisen, J.T. (2015). Deep-water sediment bypass. *Journal of Sedimentary Research*, 85, 1058-1081.

Stewart, S.A. & Reeds, A. (2003). Geomorphology of kilometre-scale extensional fault scarps: factors that impact seismic interpretation. *AAPG Bulletin*, 87, 251-272.

Stiros, S.C., Marangou, L. & Arnold, M. (1994). Quaternary uplift and tilting of Amorgos Island (southern Aegean) and the 1956 earthquake. *Earth Planet. Sci. Letters*, 128, 65-76.

Straub, K.M. & Pyles, D.R. (2012). Quantifying the hierarchical organization of compensation in submarine fans using surface statistics. *Journal of Sedimentary Research*, 82, 889-898.

Stucky de Quay, G., Roberts, G.G., Watson, J.S. & Jackson, C.A.-L. (2017). Incipient mantle plume evolution: constraints from ancient landscapes buried beneath the North Sea. *Geochemistry, Geophysics, Geosystems*, 18, 973-993.

Tindale, K., Newell, N., Keall, J. & Smith, N. (1998). Structural evolution and charge history of the Exmouth Sub-basin, northern Carnarvon Basin, western Australia. In: P.G. Purcell & R.R. Purcell (Eds.), *The Sedimentary Basins of Western Australia 2: Proceedings of the Petroleum Exploration Society of Australia*. PESA, Perth, 447-472.

Turner, C.C. & Cronin, B.T (Eds.). (2018). *Rift-related coarse-grained submarine fan reservoirs; the Brae Play, South Viking Graben, North Sea*. AAPG Memoir, 115, 630pp.

Underhill, J.R., Sawyer, M.J., Hodgson, P., Shallcross, M.D. & Gawthorpe, R.L. (1997). Implications of fault scarp degradation for Brent Group prospectivity, Ninian Field, northern North Sea. *AAPG Bulletin*, 81, 999-1022.Veevers, J.J. (1988). Morphotectonics of Australia's northwestern margin – a review. In: P.G. Purcell & R.R. Purcell (Eds.), *The North West Shelf, Australia: Proceedings of Petroleum Exploration Society of Australia Symposium*. PESA, Perth, 651pp.

Walsh, J.J. & Watterson, J. (1988). Analysis of the relationship between displacements and dimensions of faults. *J. Struct. Geol.,* 10, 239-247.

Wang, Y., Straub, K.M. & Hajek, E.A. (2011). Scale-dependent compensational stacking: an estimate of autogenic time scales in channelized sedimentary deposits. *Geology*, 39, 811-814.

Watkins, S.E., Whittaker, A.C. Bell, R.E., McNeill, L.C., Gawthorpe, R.L., Brooke, S.A.S. & Nixon, C.W. (2018). Are landscapes buffered to high-frequency climate change? A comparison of sediment fluxes and depositional volumes in the Corinth Rift, central Greece, over the past 130 k.y. *GSA Bulletin*, 131, 372-388.

Welbon A.I.F., Brockbank P.J., Brunsden D. & Olsen T.S. (2007). Characterizing and producing from reservoirs in landslides: challenges and opportunities. In: Jolley S.J., Barr D., Walsh J.J. & Knipe R.J. (eds) *Structurally Complex Reservoirs*. Geological Society, London, Special Publications, 292, 49-74.

Widess, M.B. (1973). How thin is a thin bed? *Geophysics*, 38, 1176-1180.

Williams, R.M. (2018). Derisking the Thebe Disovery through cognitive interpretation. *First Break*, 36, 71-78.Whittaker, A.C., Attal, M. & Allen, P.A. (2010). Characterising the origin, nature and fate of sediment exported from catchments perturbed by active tectonics. *Basin Research*, 22, 809-828.

Yeates, A.N., Bradshaw, M.T. & Dickins, J.M. (1987). The Westralian Superbasin: an Australian link with Tethys. In: K.G. McKenzie (Ed.), *Shallow Tethys, vol. 2*. A. A. Balkema, Rotterdam, Netherlands, 199-213.

Yielding, G., Badley, M.E., Roberts, A.M. (1992). The structural evolution of the Brent Province. *Geological Society, London, Special Publications*, 61, 27-43.

Young, M.J., Gawthorpe, R.L. & Sharp, I.R. (2002). Architecture and evolution of syn-rift clastic depositional systems towards the tip of a major fault segment, Suez Rift, Egypt. *Basin Research*, 14, 1.23.

12. Figures

Figure 1
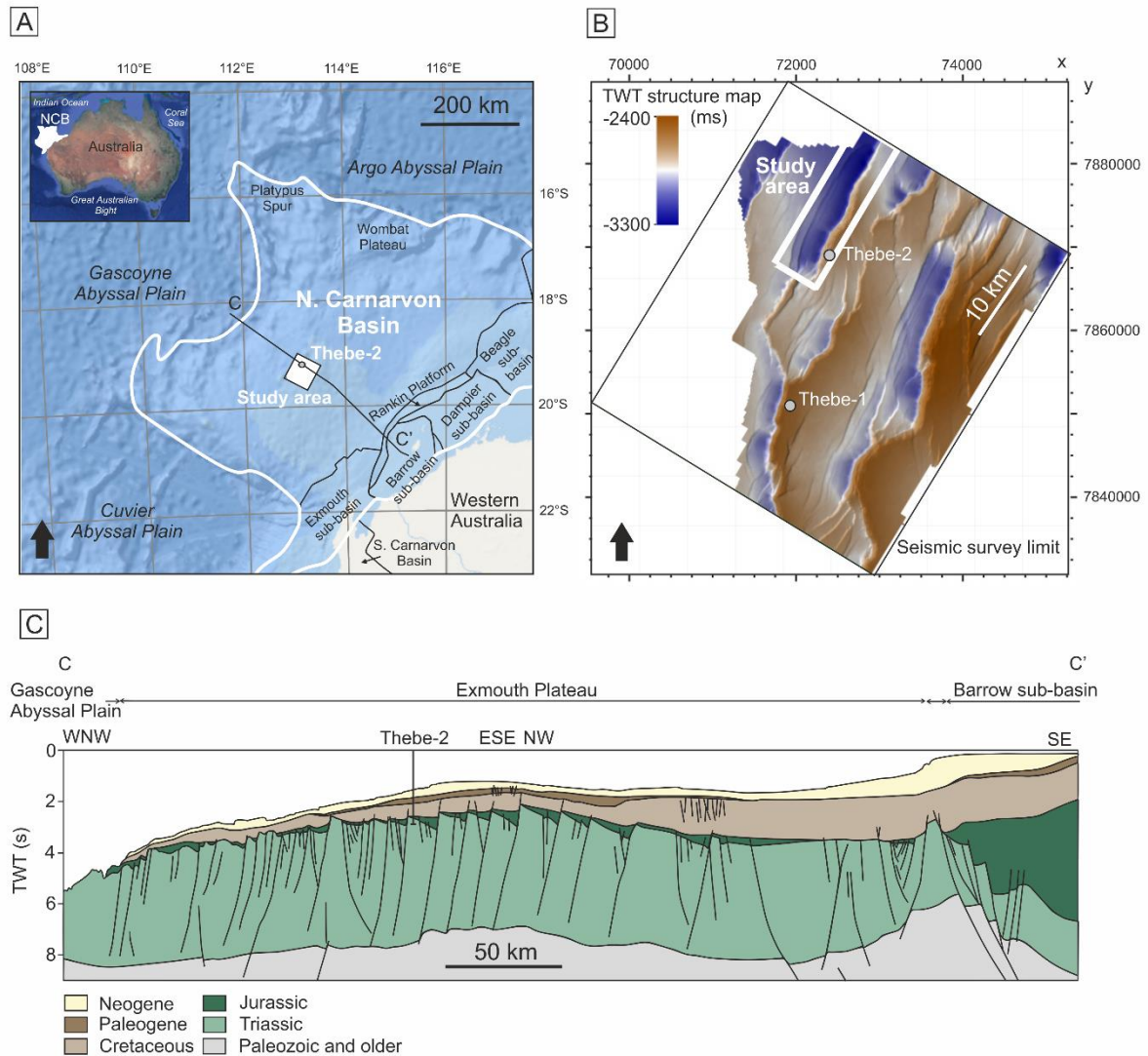
Figure 1. Study area location. A) Regional map of the NW Shelf, Australia. White box indicates study area. B) Map to show the limit of the seismic dataset. A time structure map (TWT) of the Top Pre-Rift surface is presented to highlight the faults. The specific study area covers the most north-western fault block; the Thebe-2 well penetrates the footwall of the fault. C) Regional schematic dip-section, with the position of the Thebe-2 well (modified from Geoscience Australia). Section position shown in A (C-C').

Figure 2
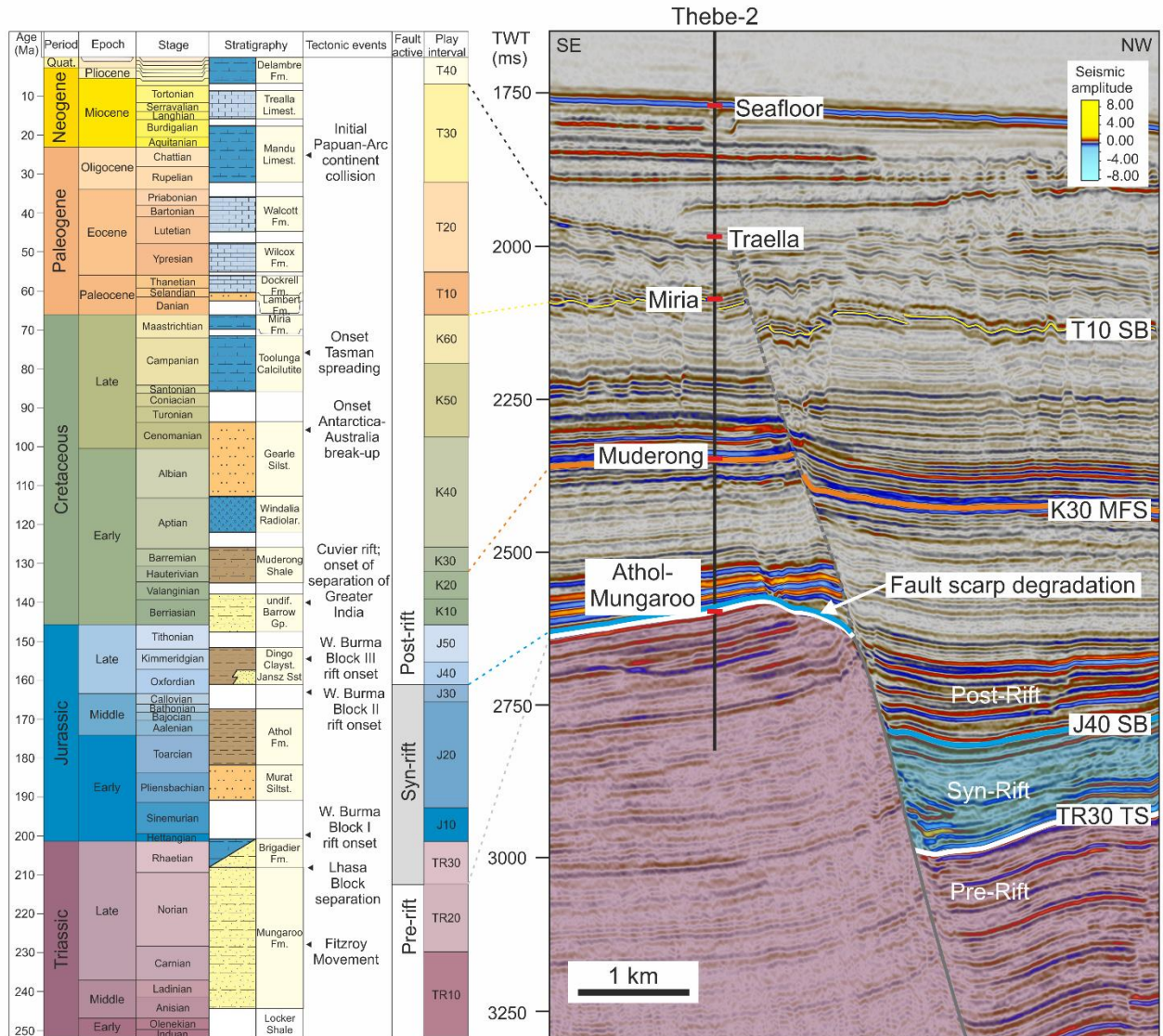
Figure 2. Stratigraphy of the northern Carnarvon Basin with formation tops from the Thebe-2 well presented on a NW-SE seismic section. The syn-kinematic interval of this fault is between the TR30 transgressive surface and J40 sequence boundary, which is expressed as a vertical succession in the hangingwall (blue shading), and a surface in the footwall. Pre-rift stratigraphy is shaded in pink. TS = Transgressive surface; MFS = Maximum flooding surface; SB = sequence boundary. Tectonic events from Longley et al. (2002). Play intervals from Marshall & Lang (2013).

Figure 3
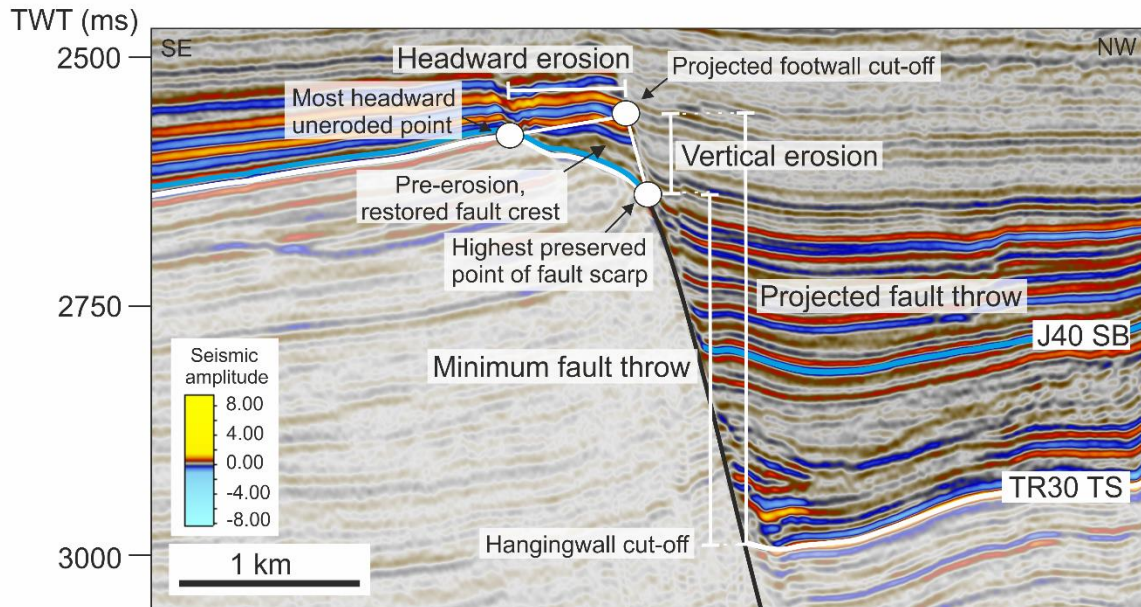
Figure 3. Positions on the fault that are used for measuring fault throw, and headward and vertical erosion, associated with fault scarp degradation. Pre-rift stratigraphy is shaded translucent white.

Figure 4
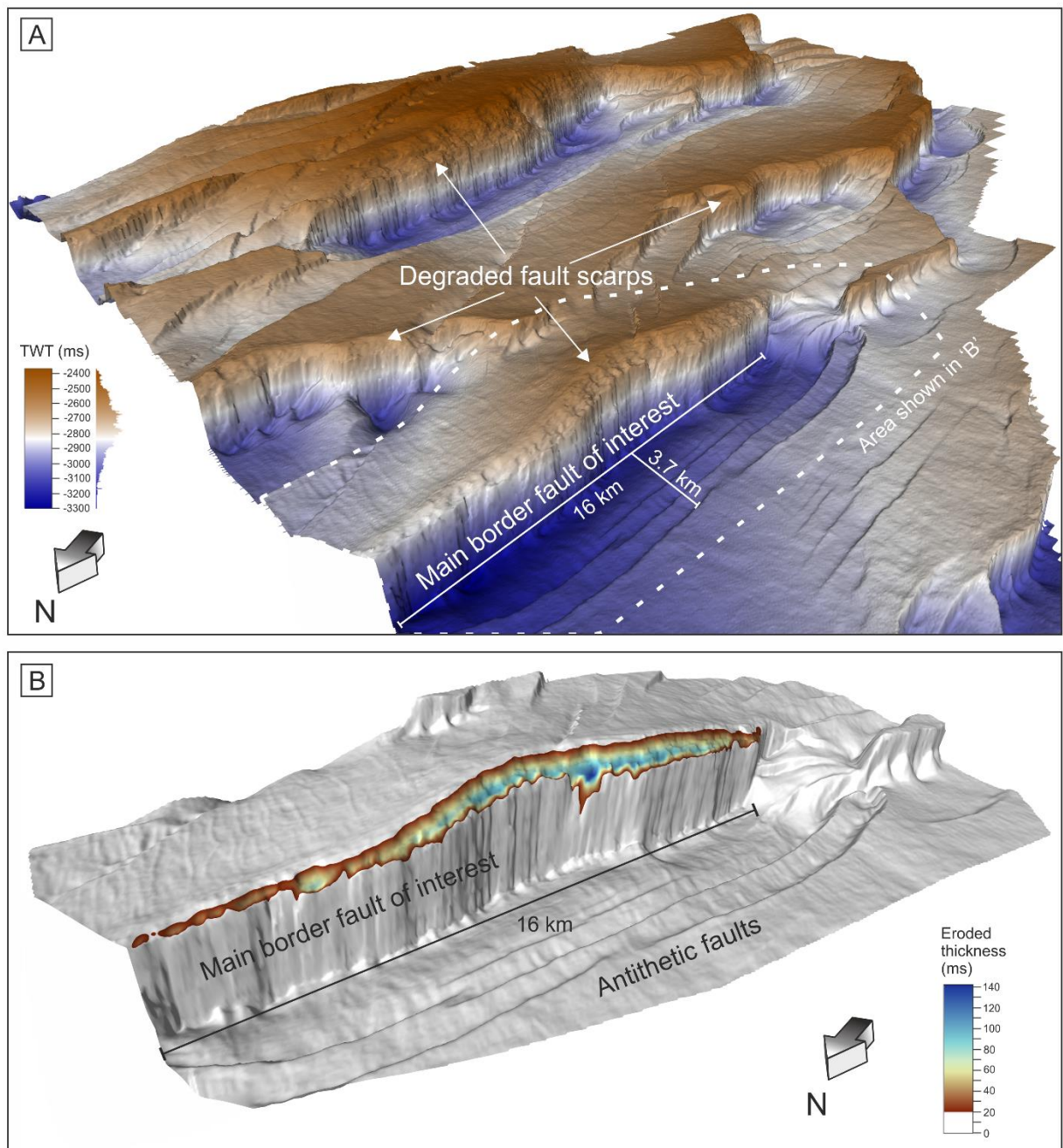
Figure 4. A) 3D capture of the Top Pre-Rift surface across the seismic dataset to reveal a series of normal fault blocks with degraded fault scarps. B) 3D image of the fault of interest in the study area (position shown in 'A' with white dashed outline). A map of the eroded thickness of sediment is overlain onto the fault scarp. Eroded thickness colour map from Crameri (2018).

Figure 5
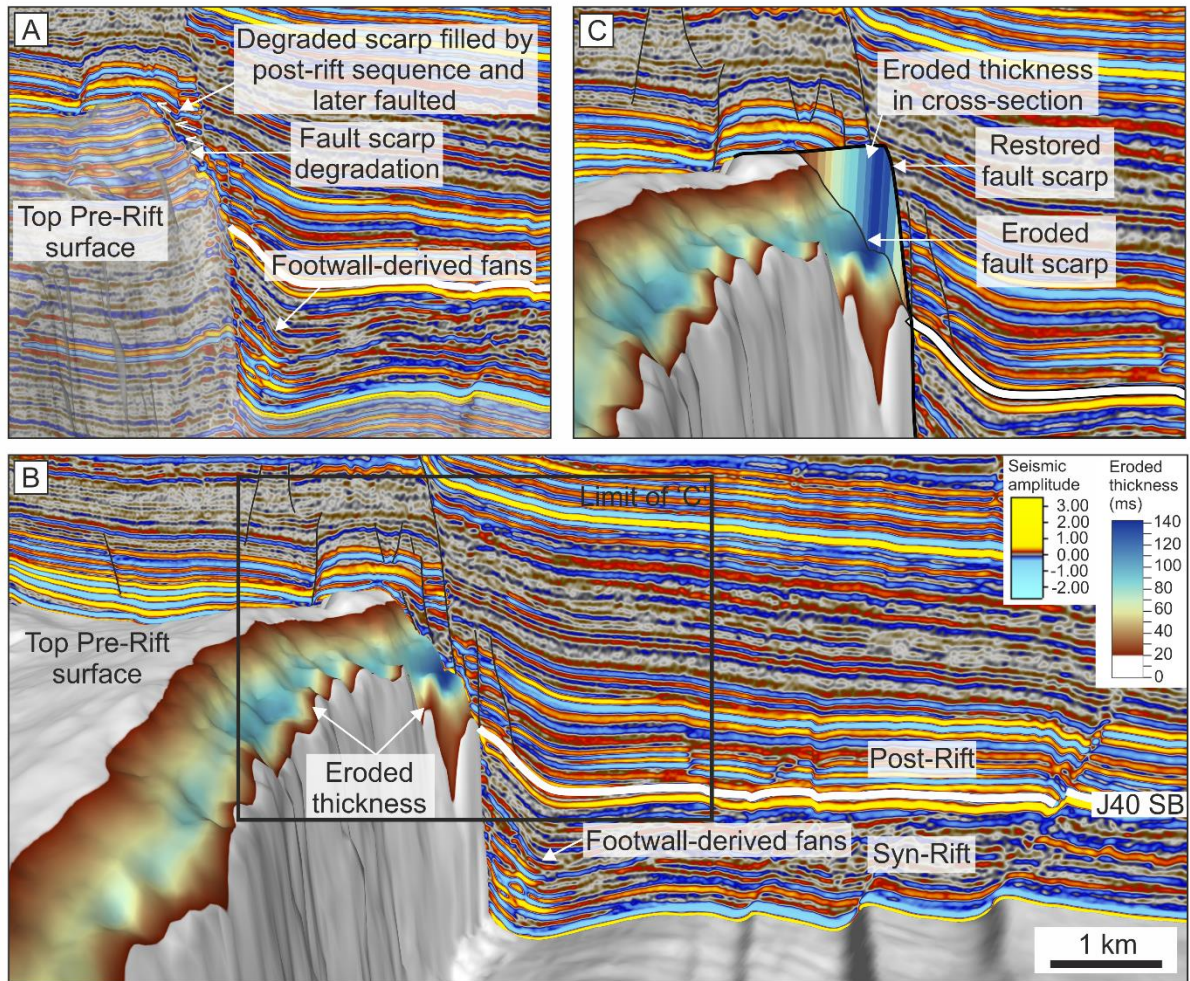
Figure 5. Seismic cross-section to highlight the degraded fault scarp. A) Degraded area of the fault scarp is onlapped and filled by the post-rift strata. Transparency is applied to the Top Pre-Rift surface to reveal the footwall seismic character. B) Map of the eroded thickness of sediment is overlain onto the fault scarp. C) Zoomed in area of 'B' to show eroded thickness of the footwall projected onto the seismic cross-section. SB = sequence boundary. Eroded thickness colour map from Crameri (2018).
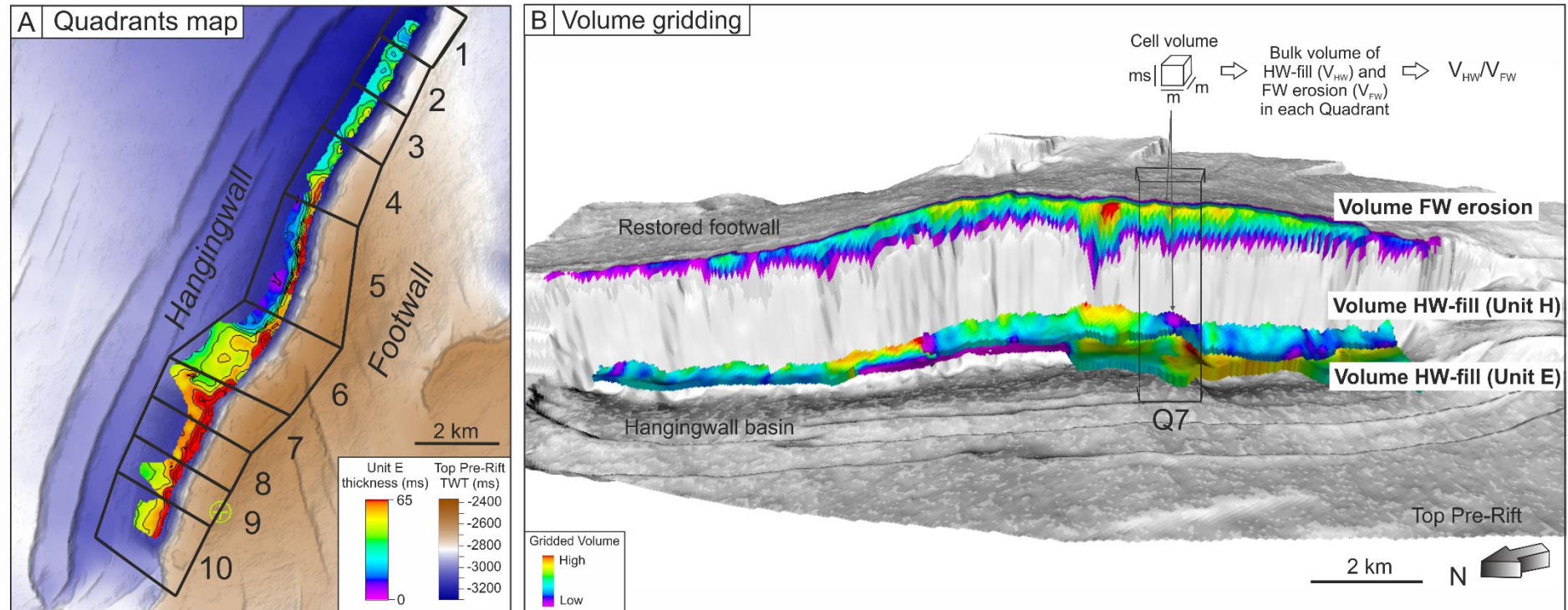
Figure 6. Methodology for volume balancing approach (V_{HW}/V_{FW}). A) Layout of quadrants along the fault for analysis. Quadrant boundaries are defined by interfan areas in the hangingwall basin, demonstrated here with an isochron map of Unit E containing footwall-derived fans. Each quadrant encompasses an area of the footwall and hangingwall. B) Volume gridding approach of the hangingwall units (Units E and H) containing footwall-derived fans, and eroded material from the footwall. The restored footwall to its pre-erosional state is presented. HW = hangingwall; FW = footwall.

Figure 7

A

Seismic TWT (ms)

0 — MSL

Seabed
1870 ⋯ ⋯ 1430 mMD
Average vel.
762 ms from checkshots
below seabed
787 m

2066 m/s

2632 — Top Pre-Rift
2217 mMD

Check average vel. data
at TPR using seismic
TWT and MD:

(D/T) x 2 = (787/0.762) x 2
= 2065.62 m/s

Footwall cell height

1 ms
TWT
1 m
1 m
1 m

D = V x T = (2066/0.001)
= 2.066 m

Height of grid cell = D/2
= 1.033 m

B

Thebe-2
Interval velocity (m/s) | Average velocity (m/s)

TWT (ms)

2500

2600

2700

2800

2900

3000

3100

V_{FW} cell volume
1.09 m | 1 m / 1 m

V_{FW} cell volume
1.03 m | 1 m / 1 m

Cell volumes
in calculation
1 m
(1 ms) | 1 m / 1 m

Seismic
amplitude
8.00
4.00
0.00
-4.00
-8.00

2182 m/s

2064 m/s

Top Pre-Rift
Gas column

Extrapolate
interval vel.

Extrapolate
average vel.

J40 SB

2363 m/s

2282 m/s

Velocities at depth
of top of hangingwall fans

V_{HW} cell volume
1.14-
1.18 m | 1 m / 1 m

1 km

Figure 7. Approach for validating cell volume equivalency between the footwall (where there is velocity data from the Thebe-2 well) and the hangingwall (where there is no velocity data). 1 ms (TWT) is assumed to represent 1 m vertical height of a cell for both footwall and hangingwall intervals in volume calculations; here we check if that assumption is valid. A) Approach for calculating grid cell height in the footwall using the average velocity trend from checkshot data (1.03 m). Average is taken from the first checkshot to the Top-Pre-Rift surface and is verified using seismic TWT data and the measured depth (MD) in the well. TWT = two-way time; TPR = Top Pre-Rift surface; D = distance; V = velocity; T = time. B) Approach for calculating grid cell height in the hangingwall. Velocities are extrapolated from to the depth of the hangingwall fans using the velocity trends from the seabed to the Top Pre-Rift surface, thus excluding the pre-rift succession and gas-bearing sediments from the trend. This gives vertical cell heights of 1.14-1.18 m for the hangingwall fans. Various assumptions are inclusive of this approach (see text). Hangingwall cell volumes are thus shown to be underestimated by up to 15% relative to footwall cell volumes in the approach, hence volume balance estimates represent minimum values.

Figure 8A
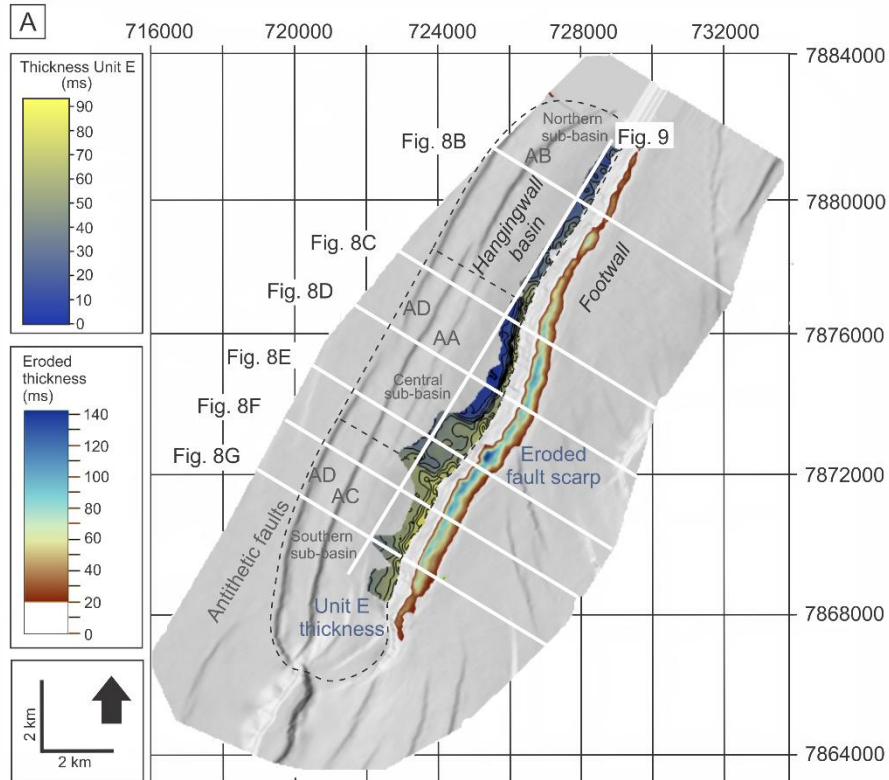
Figure 8. Six NW-SE trending representative seismic sections along the fault are presented to show the stratigraphic framework. A) Map of the basin (Top Pre-Rift surface) to show positions of seismic sections (B-G). A map of the eroded thickness of the fault scarp is overlain onto the footwall and an isochron map of Unit E is presented in the hangingwall. The basin is divided into three sub-basins for reference; northern, central and southern. Antithetic faults AA-AD are highlighted. Sections B-G: uninterpreted and interpreted seismic sections. Pre-rift stratigraphy is shaded white. Seismic units A-L are shaded in blues. Footwall degradation is shaded in black on interpreted sections. Key stratal surfaces (KSS) are highlighted in white. Eroded thickness colour map from Crameri (2018).
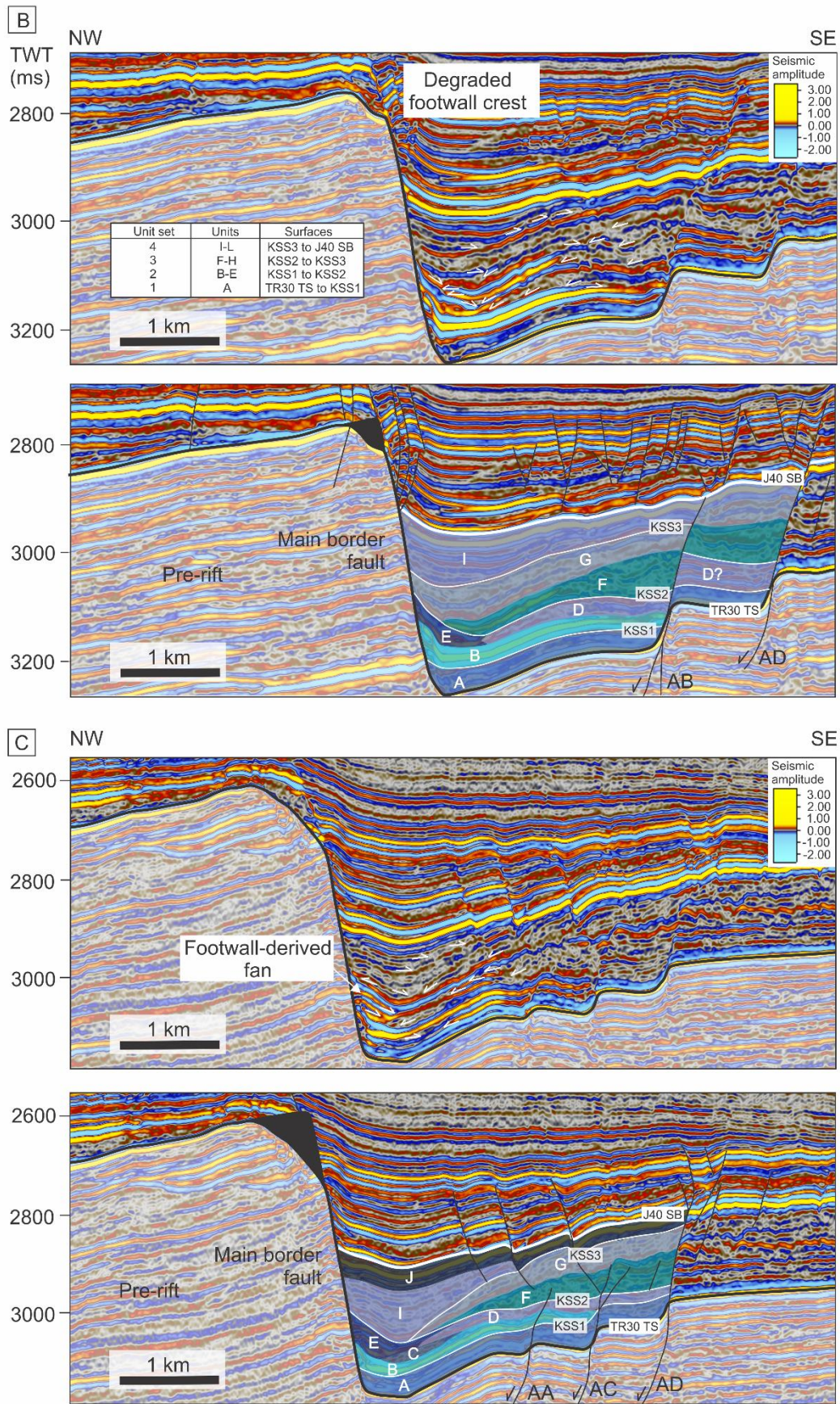
Figure 8B & C
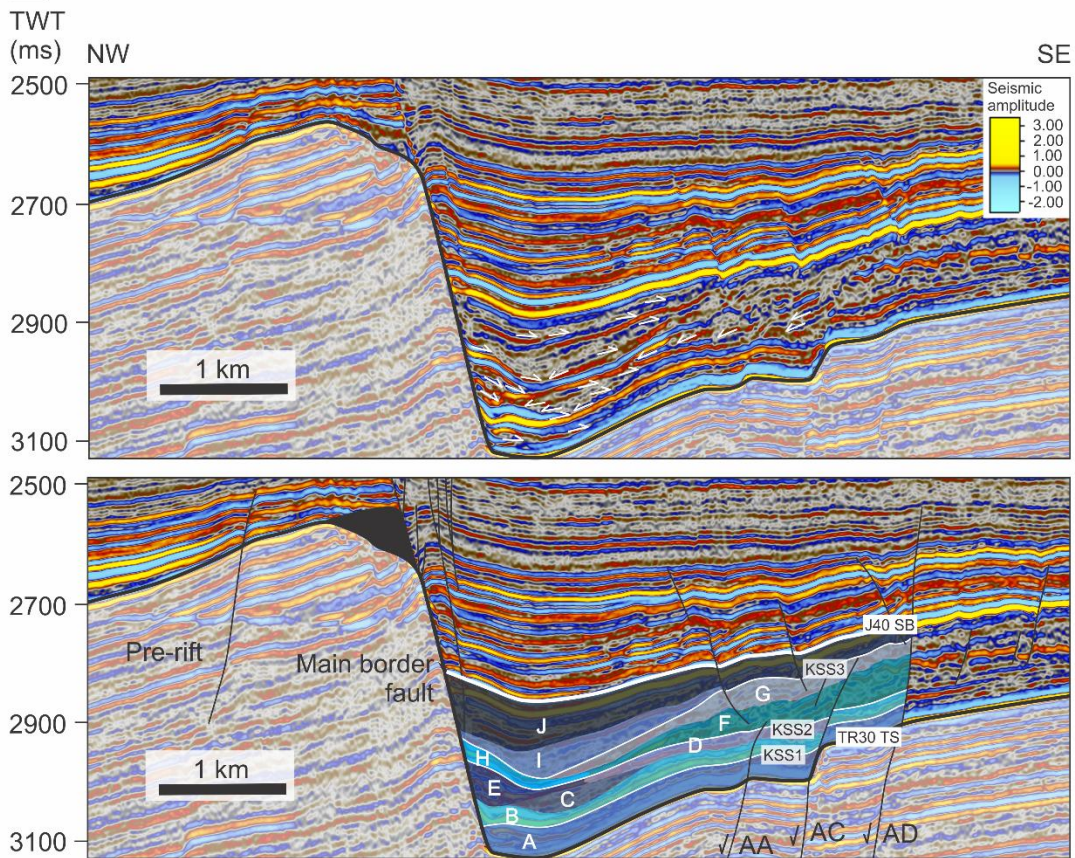
Figure 8D & E
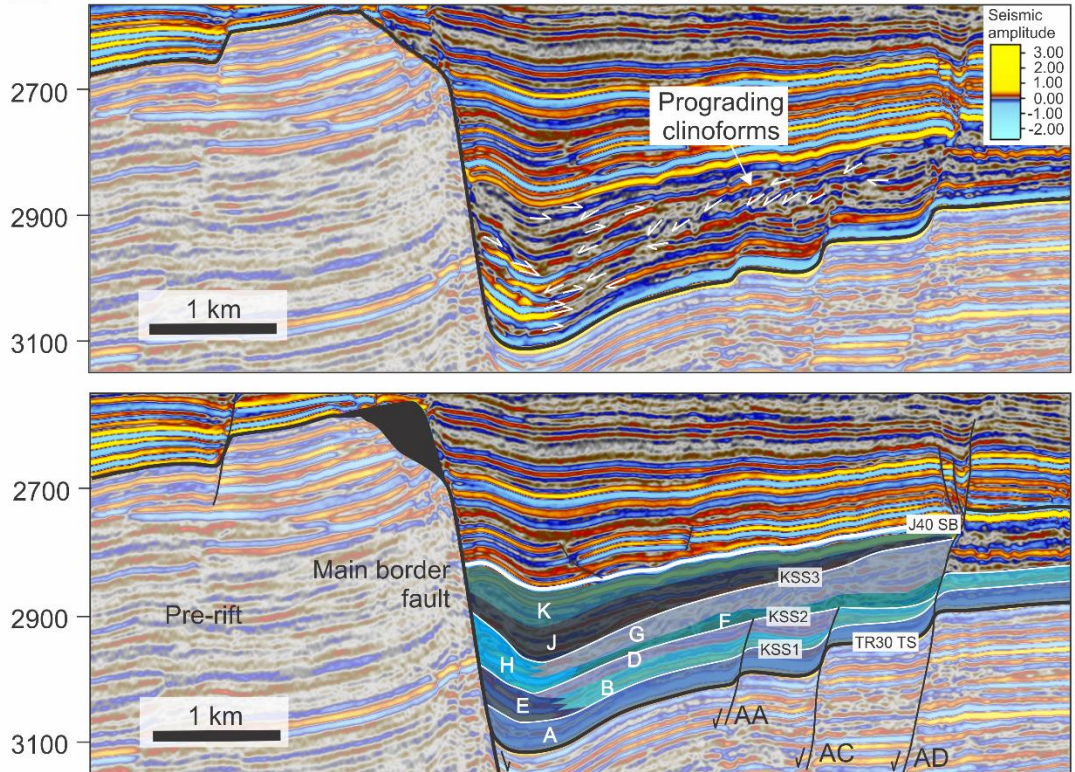
Figure 8F & G
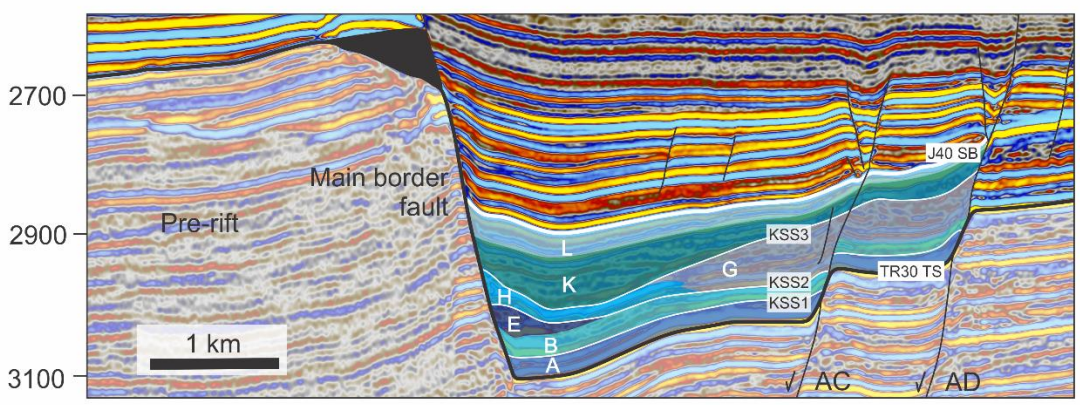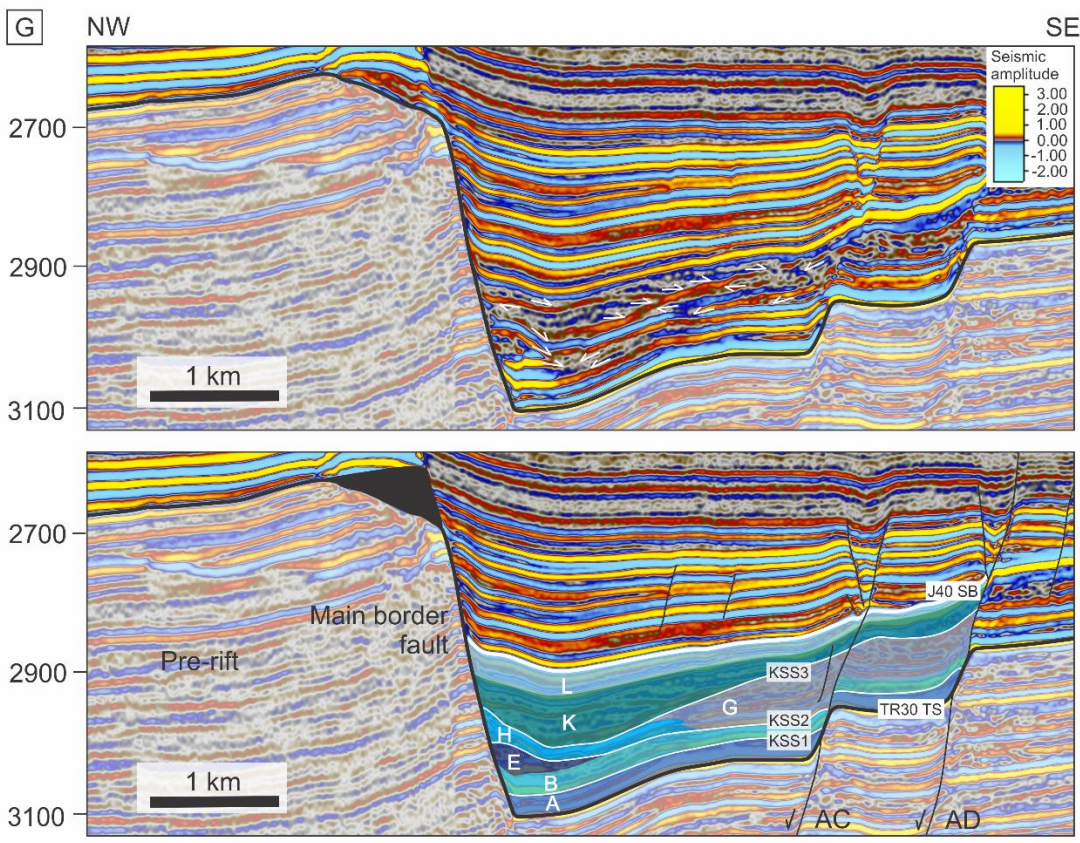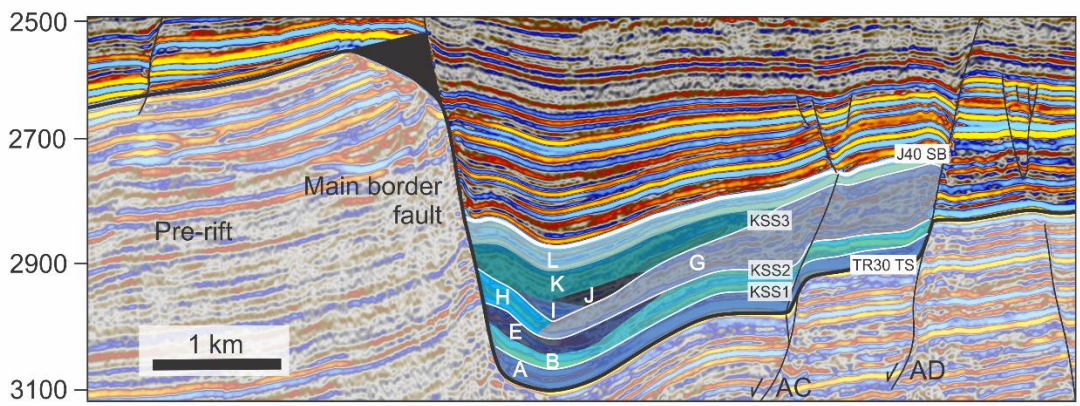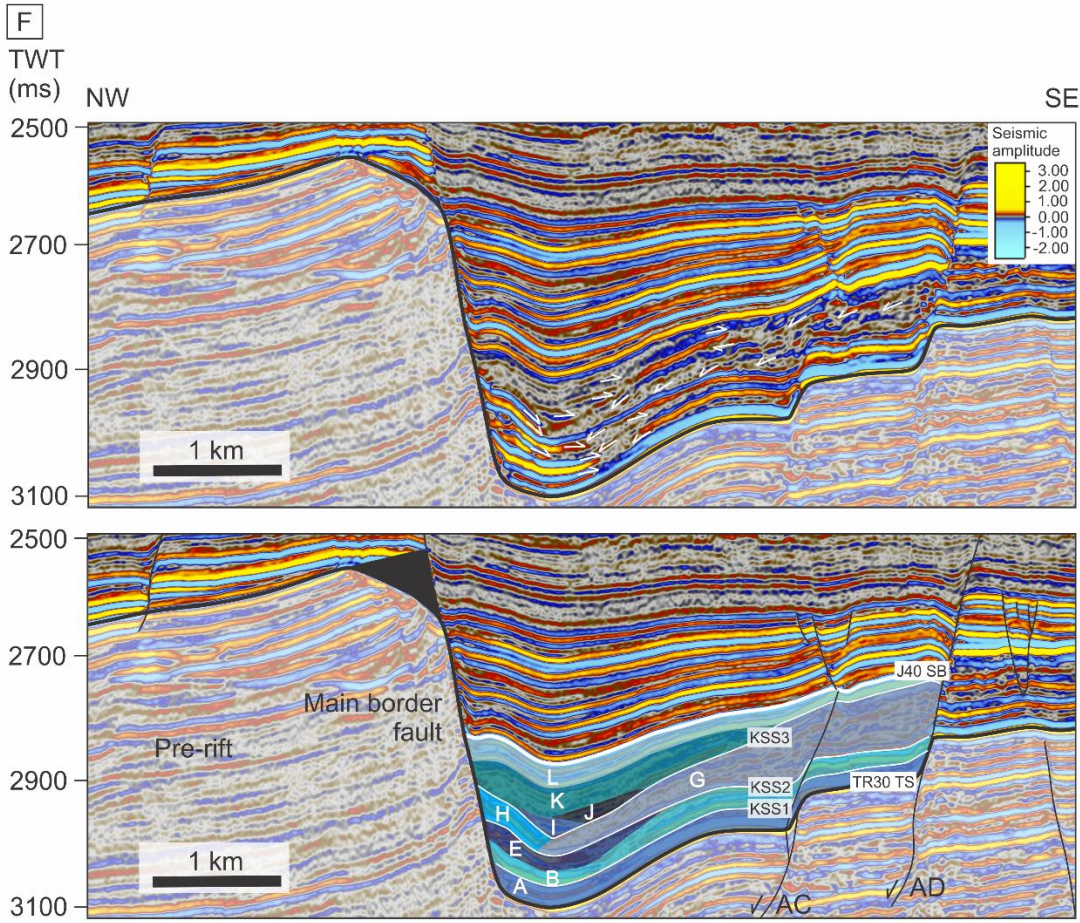
Figure 9
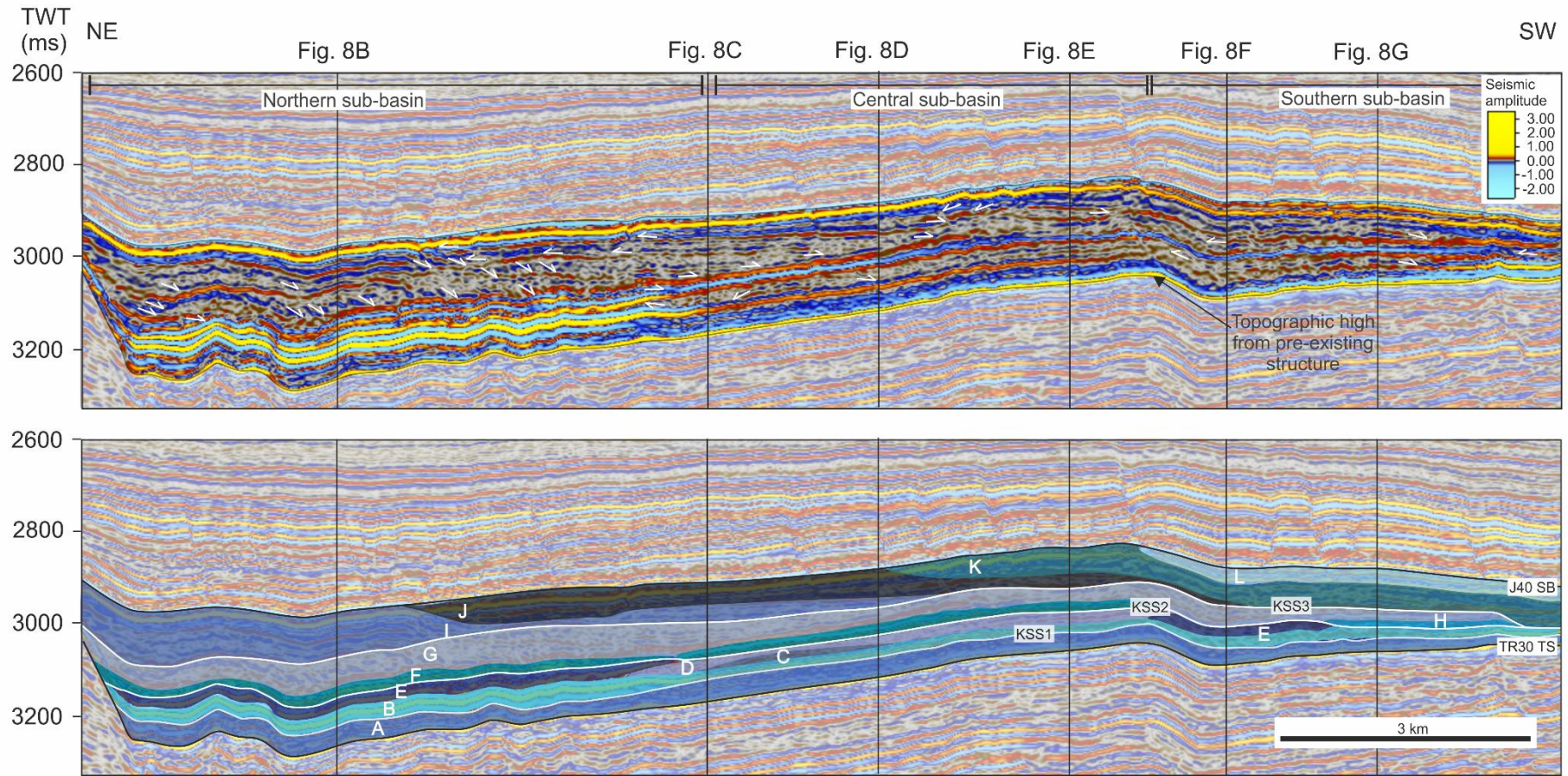
Figure 9. Representative strike section (NE-SW) through the hangingwall stratigraphy with clean and interpreted seismic data. The stratigraphic framework is shaded in blues (Units A-L). Key stratal surfaces (KSS1-3) are highlighted with white lines. Pre-rift stratigraphy is shaded white. Position of section is indicated in Figure 8A and is proximal to the main border fault. Positions of Fig. 8 dip sections, sub-basin extent and position of topographic high between the central and southern sub-basins are indicated.

43
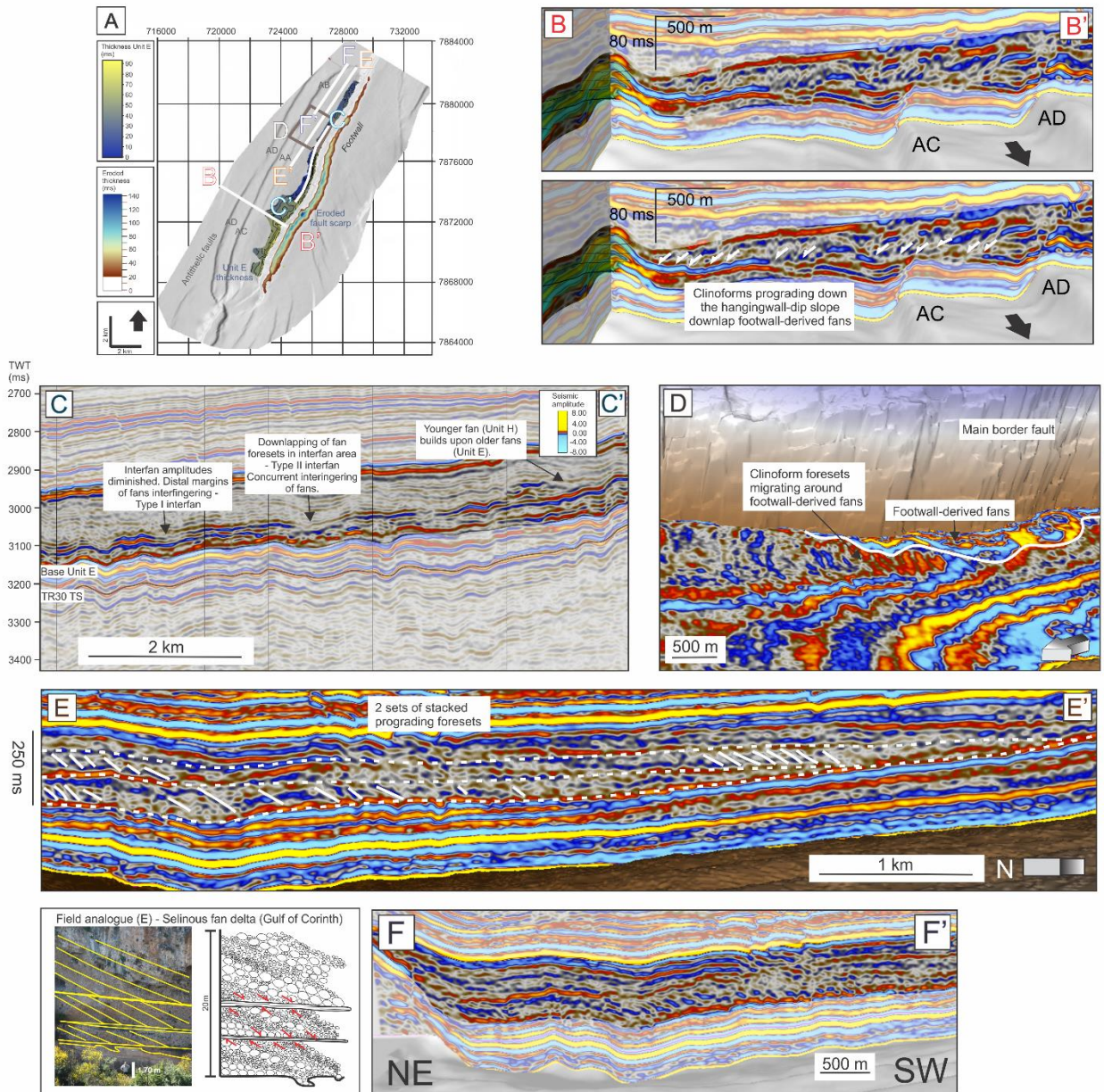
Figure 10

Figure 10. Architectural variability and geometric relationships between depositional systems across the basin. A) Map of the basin with positions of sub-plots. B) Clinoforms prograding down the hangingwall dip-slope and downlapping footwall-derived fan margins. C) Strike section through footwall-derived fans showing interfan variability (interfan scheme according to Barrett et al., 2019b). D) Amplitude time-slice to show axial-derived foresets migrating around footwall-derived fans. E) Cross-section to show two sets of axial-derived, stacked foresets that prograded from NE fault tip. Field analogue of (E) from the Selinous fan delta (Gulf of Corinth, Greece) is highlighted (Barrett et al., 2019a). F) Alternative, clean cross-section to show foresets prograding from NE fault tip. Uninterpreted versions of the seismic sections in the Appendix.
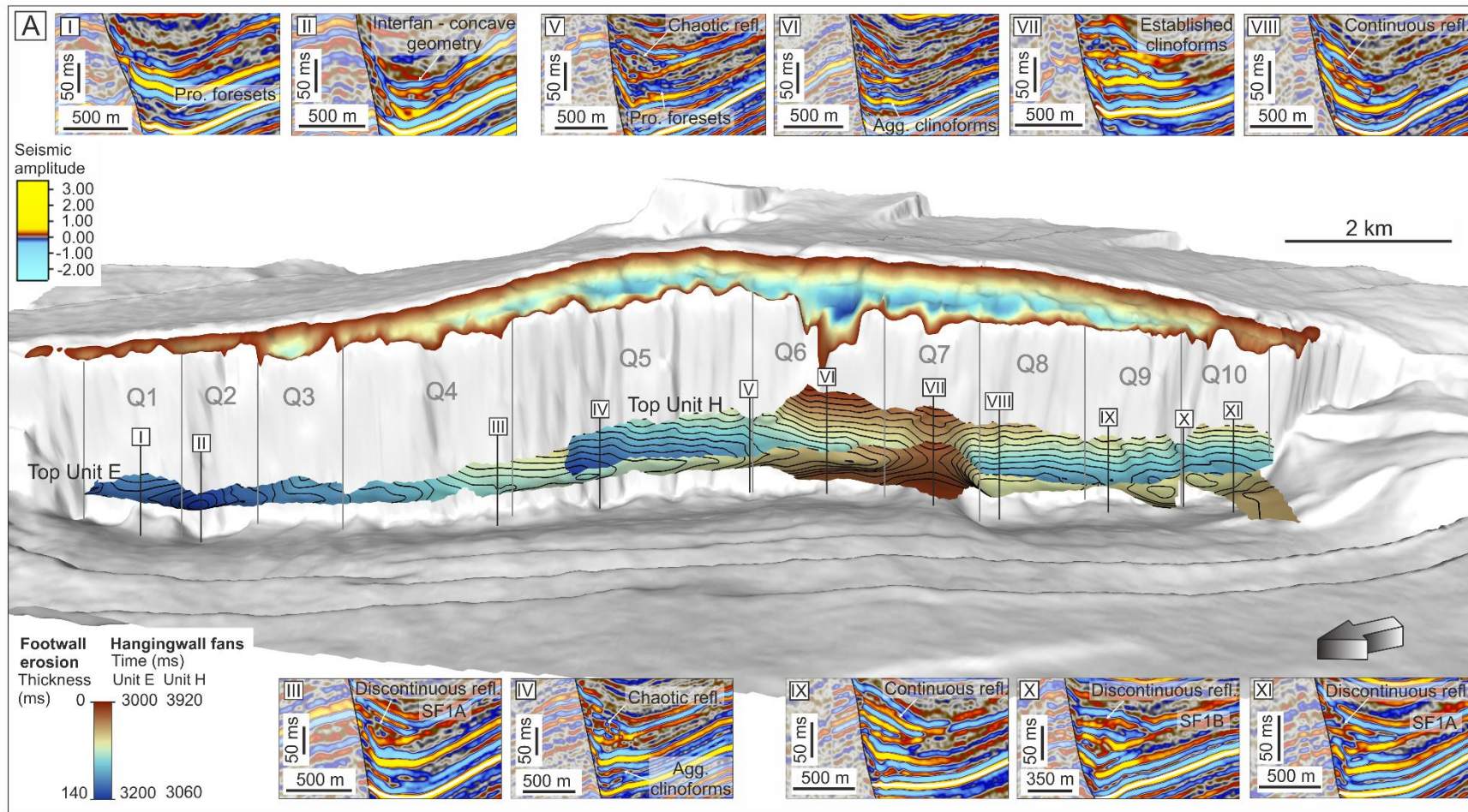
Figure 11. Along-strike variability of footwall-derived fans. A) Top surfaces of Units E and H in the hangingwall are presented with the amount of fault scarp erosion overlain onto the footwall. Positions I-XI show the substantial variability in fan character and geometry along the fault. Quadrants 1-10 are highlighted. B) Focus upon three positions (VI-VIII) to show internal variability and stacking within the fans through the vertical succession. Eroded thickness colour map from Crameri (2018).
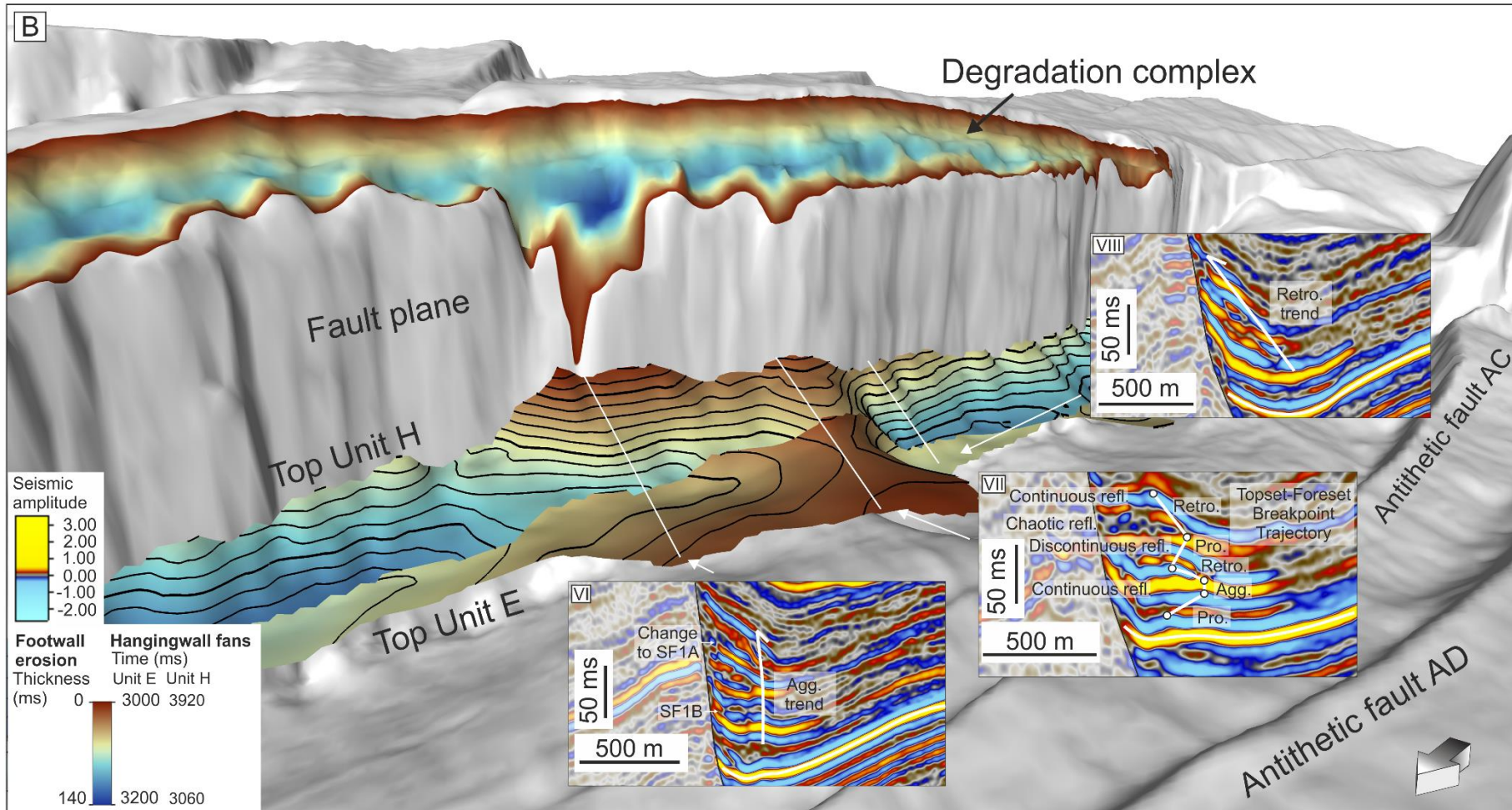
Figure 11B
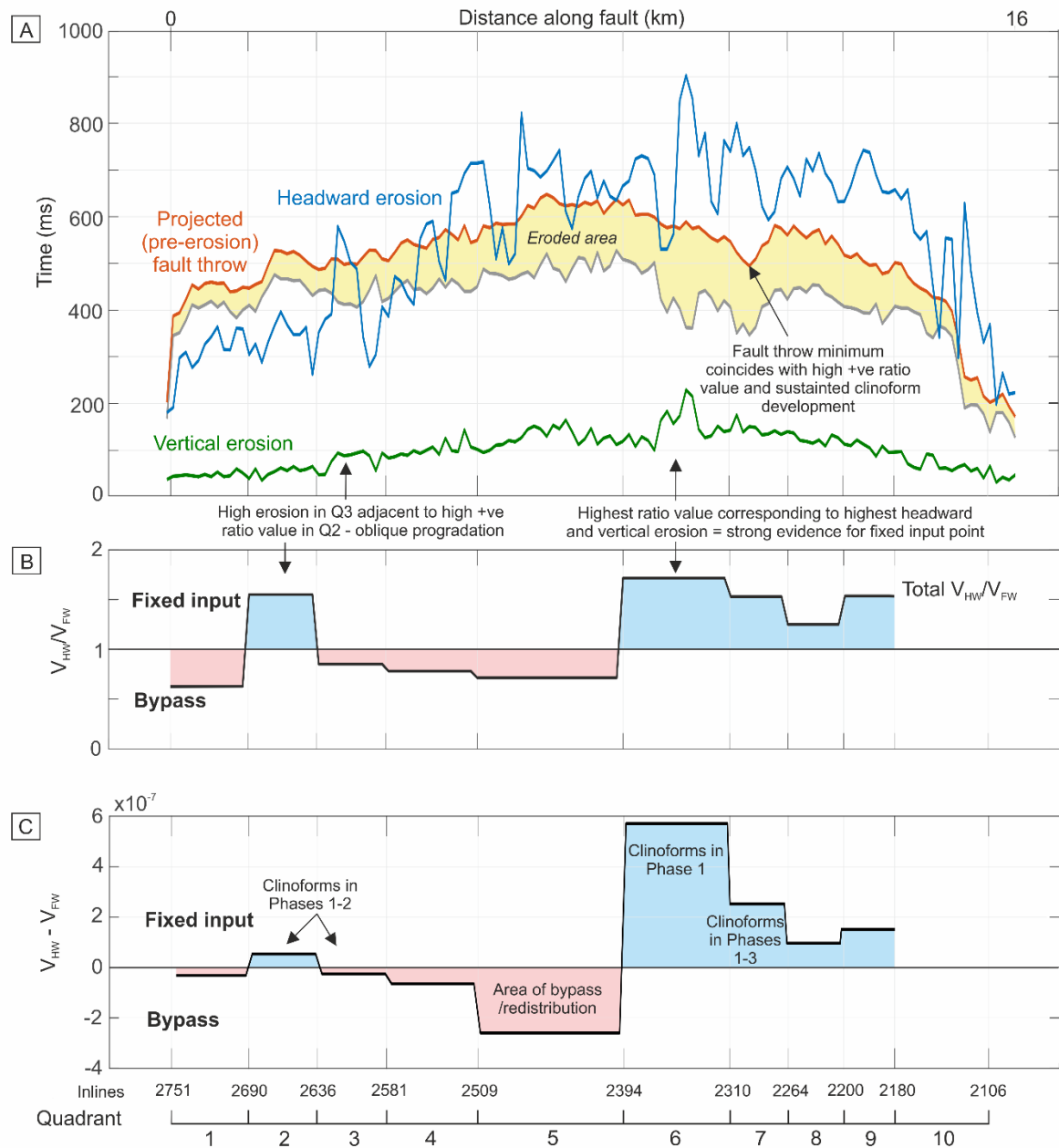
Figure 12. Graphs to show results of the footwall analysis and volume balancing. A) Fault throw from the restored footwall (red) and from the preserved state of the fault (grey). Yellow shaded area represents amount of vertical erosion, which is also plotted in green. Vertical (green) and headward erosion (blue) vary along-strike but generally follow the parabolic trend of the fault throw distribution. B) Ratio of hangingwall fill of footwall-derived fans to footwall erosion (V_{HW}/V_{FW}). Values below 1 represent excess footwall erosion, i.e. areas of sediment bypass. Values greater than 1 represent areas of excess hangingwall fill, i.e. positions of through-going sediment input points. C) Plot to show V_{HW}-V_{FW}, which accounts for quadrant size. The largest positive ratio peak is in Quadrant 6, which coincides with the highest values of headward and vertical erosion, and clinoform development in Phase 1. The high, positive ratio value in Quadrant 7 coincides with the fault throw minimum and clinoform development in Phases 1-3. High headward and vertical erosion in Q3 occurs adjacent to a high positive ratio value in Q2, which suggests oblique progradation. This is confirmed with seismic mapping, e.g. Top Unit E contours in Fig. 11A.

Figure 13
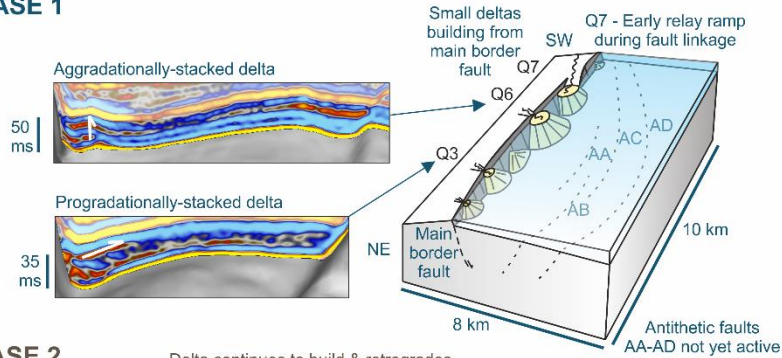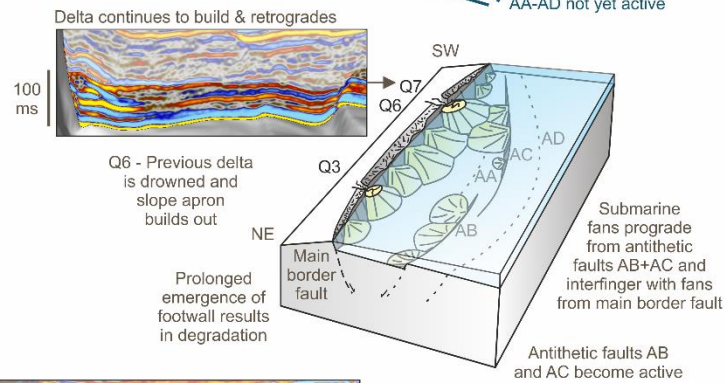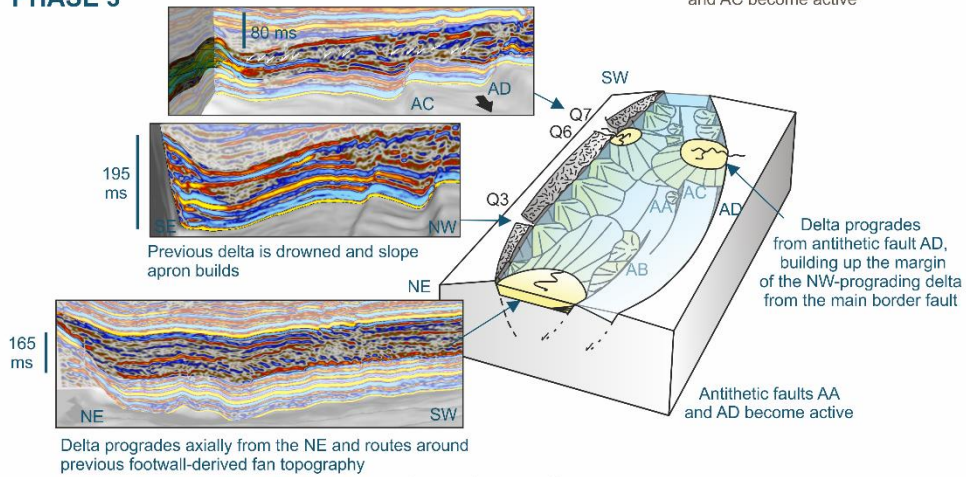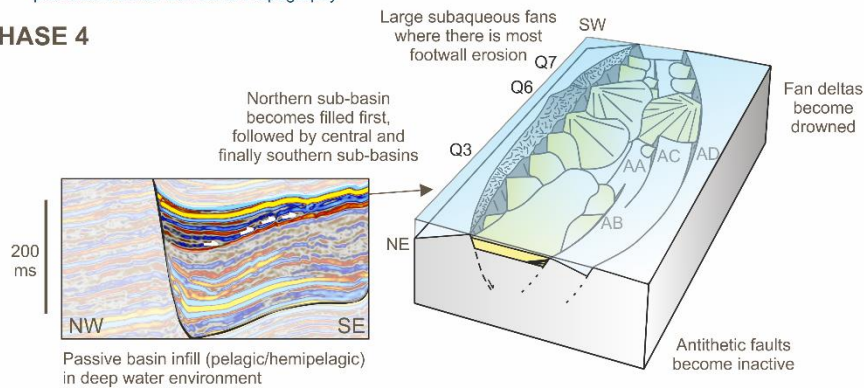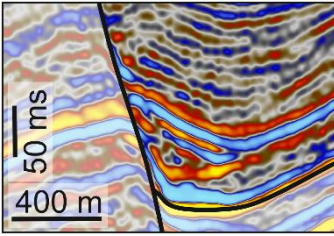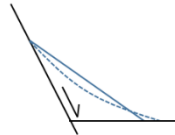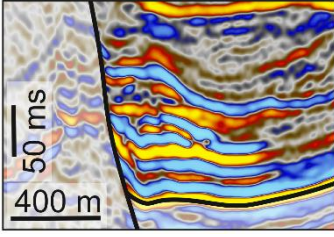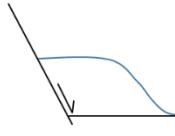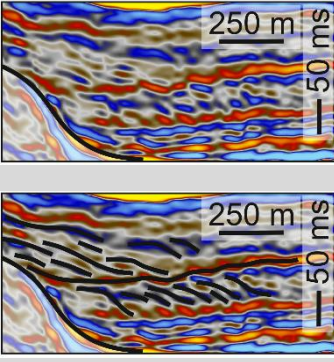
Figure 13. Block models to show the tectono-sedimentary evolution of the basin from Phases 1-4. Representative seismic extracts are shown to highlight evidence for interpretations. Antithetic faults AA-AD are indicated.

Table 1. Seismic facies: example extracts, descriptions and interpretations.

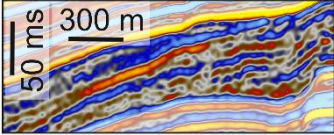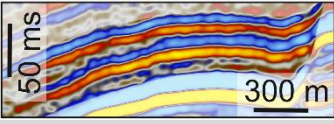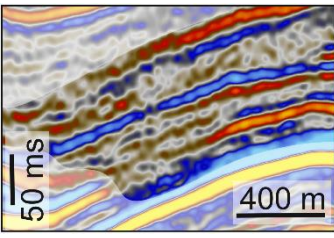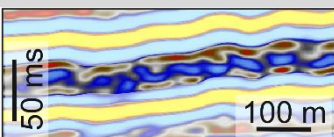| Seismic facies	Example	Description	Interpretation
SF1	a) b)	*Character:* Mainly high amplitude, low-med. frequency (10-50 Hz), steeply-dipping reflections. Internal reflections range from continuous to chaotic. *Geometry:* a) Planar-slightly concaved slope. 3D prism-apron shape along the fault. No radial geometry. b) Flat-slope clinoform. 3D radial geometry and in some cases interfingering with adjacent fans. Foreset heights ranges from 40 ms-200 ms (70-350 m with 1742 m/s velocity). Internal architectures vary along-strike, but generally exhibit progradational stacking near the base, and aggradational or retrogradational stacking towards the tops of the fans. *Position:* Always positioned in the immediate hangingwall and dipping away from the main border fault. a) Sloping reflections continue along the fault <4 km and extend <650 m away from the fault. b) Numerous positions – most striking example is ~4.5 km from the southern end of the basin	Footwall-derived fans: a) Slope apron b) Fan delta
SF2		*Character:* Low-med. amplitude (peaks brighter than troughs), low-med. frequency (10-50 Hz), discontinuous, dipping reflections. Separated by high amplitude, flat-lying reflections that are conformable. *Geometry:* 3D radial geometry. Foreset height 20-40 ms (35-70 m with 1742 m/s velocity). Foresets exhibit a highly progradational stacking pattern. *Position:* Foresets prograde from the northern fault tip in a direction parallel to the fault trend, i.e. the depositional system follows an axial route. Foresets are restricted to a single interval/unit and are confined laterally and at their distal extent by footwall-derived fans. Only occurs in Unit G.	Stacked, prograding fan delta foresets, separated by flooding surfaces.

49
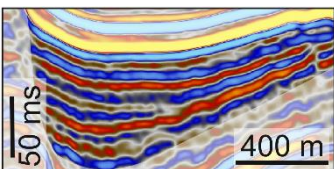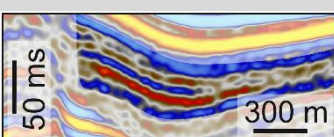
SF3		*Character:* Medium amplitude, med. to high frequency (40-70 Hz) reflections with moderate continuity. *Geometry:* Low-angle, basinward-dipping with clinoformal and radial shape. Foreset height 50-60 ms (90-105 m with 1742 m/s). Topset length <300 m. *Position:* Prograding away from antithetic faults into the southern sub-basin. Occurs only in Unit G.	Deltaic clinoforms prograding basinward from antithetic faults
SF4		Medium to high amplitude, low-med. frequency (20-50Hz), moderate-high continuity, undulating reflections that are relatively flat-lying to gently-dipping (sometimes following pre-rift topography) and fade/pinch-out down-dip and along-strike. Observed in Units A, B, D, F, K.	Turbidites?
SF5		Low amplitude, low frequency (10-20Hz), chaotic-discontinuous reflections. Apparent at the downdip terminations of higher amplitude, dipping reflections. Observed in Units B, C, D, E, F, G, H, I, K.	Mass transport deposits/hemi pelagic fall-out in clinoform bottomsets
SF6		Med. amplitude, low-high frequency (10-80Hz), discontinuous reflections with undulating geometries. Observed in the lowest syn-rift stratigraphy (Unit A).	Unknown – channels?
SF7		Med. amplitude, med.-high frequency (40-70Hz), continuous reflections, onlapping underlying topography. Some undulations. Observed in the upper part of the syn-rift stratigraphy (Units I, J, K, L).	Turbidites/ Pelagic /hemipelagic fall-out
SF8		Low to med. amplitude, high frequency (50-80Hz), steeply-dipping reflections with a planar sloping geometry that appears to be radial in 3D. Observed in Units J, L. Dipping reflections are <100 ms high.	Submarine fan?

Table 2. Stratigraphic framework: seismic unit descriptions. U = Unit.

U	Unit Set	Colour	Key features	Seismic Facies	Extent	Fault thickening	Top surface character	Max. strat. thick.	Max. foreset height
A	1		Small clinoforms from main border fault	SF6	Whole basin	Main border fault	KSS1. Bright and continuous reflection in N - becomes discontinuous towards S. Change of seismic facies across surface.	63 ms Thins toward S	20 ms
B	2		Fans from main border fault and antithetic faults	SF1a-b; SF4	Whole basin	Main border fault & AB & AC	Change of seismic facies & downlap from reflections above.	40 ms. Av. 23 ms	30 ms
C	2		East- and west-dipping, interfingeri-ng reflections	SF5	Cent. sub-basin	None	Distinct, flat-lying, high amplitude trough, downlapped by Unit E and F.	53 ms	
D	2		Depos. system from NW, antithetic faults	SF4; SF5	North. and central sub-basins. Restri-cted to the NW.	AB & AC	KSS2. In the N, downlapped by system from NW (Unit F), and towards S it is downlapped by Unit H. Change in seismic facies. In places eroded by Unit G.	80 ms Av. 43 ms	
E	2		Fans from main border fault	SF1a-b	Whole basin	Main border fault	KSS2. In the N, downlapped by system from NW (Unit F), and towards S it is downlapped by Unit H. Change in seismic facies. In places eroded by Unit G.	93 ms	67 ms
F	3		Depos. systems from the NW, antithetic faults	SF8; SF4; SF5	North. and central sub-basins. Restri-cted to the NW.	AA, AB, AC & AD	Downlapped by Unit G from the NW. Change in seismic facies.	80 ms	40 ms
G	3		Axial clinoforms between flat-lying reflections	SF2; SF3; SF4	Whole basin	AA, AB, AC & AD	KSS3. Onlapped by Units I, J, K, in places onto a high-amplitude approximately	86 ms; Av. 41 ms	20-40 ms

			& fans from NW, antithetic faults				flat-lying trough. Change in seismic facies.		
H	3		Fans from main border fault	SF1a-b	Cent. and south. sub-basins. Restricted to SE.	Main border fault	KSS3. Onlapped by Units I, J, K, in places onto a high-amplitude approximately flat-lying trough. Change in seismic facies.	98 ms	98 ms
I	4		Possible clinoforms from antithetic fault AB near northern fault tip. Onlapping older reflections.	SF3; SF7	North. and central sub-basins	Main border fault	In the N sub-basin – J40 SB (high amplitude, continuous reflection). In central sub-basin – downlapped by Unit J. Change in seismic facies.	96 ms Av. 29 ms	34 ms
J	4		Possible fan from main border fault - dipping, low amp. reflections	SF8	Cent. sub-basin	Main border fault	In the central sub-basin – J40 SB (high amplitude, continuous reflection). At the basinal high, downlapped by Unit K. Change in seismic facies.	100 ms	100 ms
K	4		Shallow clinoforms from main border fault	SF3; SF5	Cent. and south. sub-basins	Main border fault	Relatively flat lying, possibly erosive, high amplitude trough. Change in seismic facies.	79 ms	35 ms
L	4		Flat-lying reflections	SF4; SF7	South. sub-basin	Main border fault	J40 SB (high amplitude, continuous reflection).	80 ms	31 ms

Appendix
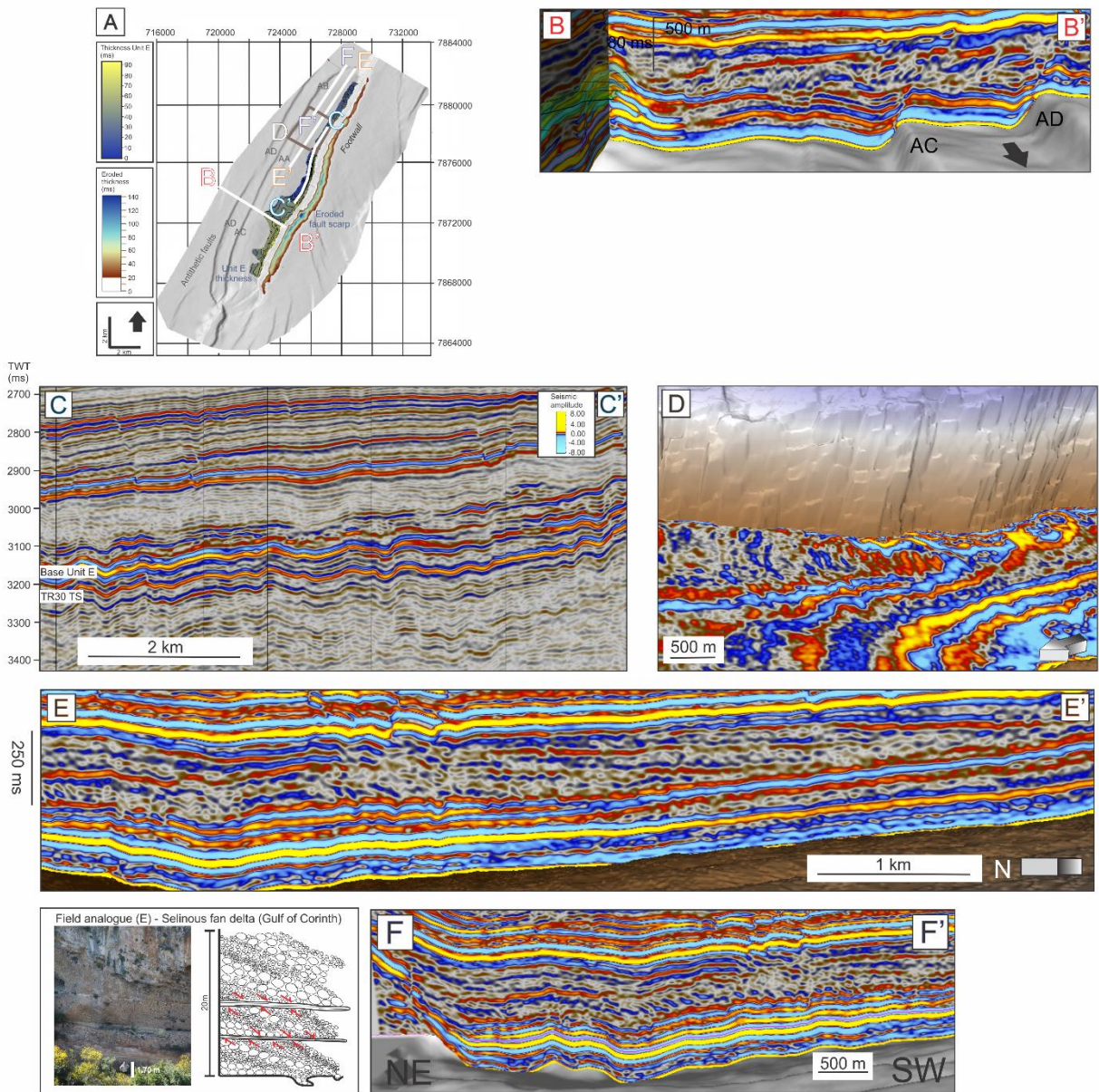
Appendix. Uninterpreted images in Figure 10 to show reflector/stratal geometries.